Evaluating convective initiation in high-resolution numerical weather prediction models using GOES-16 infrared brightness temperatures

Monthly Weather Review

David S. Henderson*

Space Science and Engineering Center,
University of Wisconsin–Madison, Madison, Wisconsin

Jason A. Otkin

Cooperative Institute for Meteorological Satellite Studies,
University of Wisconsin–Madison, Madison, Wisconsin

John R. Mecikalski

Atmospheric Sciences Department,
University of Alabama in Huntsville, Huntsville, Alabama

* Corresponding Author; David Henderson, dshenderson@wisc.edu

Abstract:

The evolution of model-based cloud top brightness temperatures (BT) associated with convective initiation (CI) are assessed for three bulk cloud microphysics schemes in the Weather Research and Forecasting model. Using a composite-based analysis, cloud objects derived from high-resolution (500 m) model simulations are compared to 5-min *GOES-16* imagery for a case study day located near the Alabama/Mississippi border. Observed and simulated cloud characteristics for clouds reaching CI are examined by utilizing infrared BTs commonly used in satellite-based CI nowcasting methods. The results demonstrate the ability of object-based verification methods with satellite observations to evaluate the evolution of model cloud characteristics, and the BT comparison provides insight into a known issue of model simulations producing too many convective cells reaching CI. The timing of CI from the different microphysical schemes is dependent on the production of ice in the upper levels of the cloud, which typically occurs near the time of maximum cloud growth. In particular, large differences in precipitation formation drive differences in the amount of cloud water able to reach upper layers of the cloud, which impacts cloud-top glaciation. Larger cloud mixing ratios are found in clouds with sustained growth leading to more cloud water lofted to the upper levels of the cloud and the formation of ice. Clouds unable to sustain growth lack the necessary cloud water needed to form ice and grow into cumulonimbus. Clouds with slower growth rates display similar BT trends as clouds exhibiting growth, which suggests that forecasting CI using geostationary satellites might require additional information beyond those derived at cloud top.

Significance Statement:

Several studies have used weather satellites to examine storm properties, however, they do not provide information about processes occurring within clouds. To address this limitation, we used numerical weather prediction model simulations and an object-based analysis method to learn more about in-cloud processes that influence the evolution of thunderstorms in the southeastern United States. The model and satellite comparison helped demonstrate that differences in the timing of rainfall formation can impact the amount of ice reaching the upper portion of the cloud. When ice forms, the cloud begins to grow rapidly and is more likely to become a long-lived thunderstorm. The results highlight the importance of using satellite data sensitive to clouds to evaluate the conditions under which cumulus clouds transition into severe storms.

1. Introduction

In the southeastern United States, the quick onset of isolated thunderstorms with heavy rainfall is commonly observed (Rickenbach at al. 2015). Accurate prediction of the onset time, location, and evolution of convection continues to be a difficult problem for observational and numerical weather prediction (NWP) models (e.g. Kain et al. 2013; Mecikalski et al. 2015; Lawson et al. 2018; Cintineo et al. 2020). When tracking growing cumulus clouds using radar and satellite observations, convective initiation (CI) is commonly referred to as the time during which growing convection contains a radar reflectivity ≥35 dBZ because that threshold is highly correlated to convection that eventually develops into a mature cumulonimbus cloud (Roberts and Rutledge 2003; Mecikalski et al. 2006). CI in the southeastern United States, particularly during the spring and summer months, can be complicated to forecast as cumulus clouds are often more isolated, and driven primarily by strong surface heating (Gambill and Mecikalski 2011; Miller and Mote 2017; Kirshbaum et al. 2016; Rickenbach et al. 2020). Such isolated weakly-forced thunderstorms can also can be initiated by subtle variations in surface heating and evaporation caused by land-use variations and topography (Gambill and Mecikalski 2011) and by small lakes (Asefi-Najafabady et al. 2012). Once convection begins, subsequent isolated convective cells typically are initiated by outflow boundaries from the surrounding convection (Goggins et al. 2010).

To help mitigate difficulties in forecasting the onset of CI, several methodologies have been developed to make use of geostationary satellite platforms to improve CI nowcasting lead times (Roberts and Rutledge 2003; Mecikalski and Bedka 2006; Mecikalski et al. 2010; Sieglaff et al. 2011; Walker at al. 2012). Along with these tracking methods, implementing combinations of the

satellite brightness temperature (BTs) and their tendencies, or so-called satellite-based interest fields, have been developed to aid the prediction of CI and the onset of heavy precipitation and lightning (e.g. Mecikalski and Bedka 2006; Harris et al. 2010). However, even when using auxiliary information about the environmental conditions, false positive detection remains an issue (Mecikalski et al. 2015). The higher spatial and temporal resolution available from the current generation of geostationary satellites have demonstrated improvements in describing the evolution of cloud characteristics associated with intense convection (e.g., Senf and Deneke 2017; Apke et al. 2018). Senf and Deneke (2017) and Patou et al. (2018) demonstrated that tracking cloud-top cooling and cloud-top hydrometeor phase are important factors when identifying clouds that will likely transition to heavy precipitation. Patou et al. (2018) and Mecikalski et a. (2015) demonstrated that connecting tracked-cloud features in satellite observations with output from NWP model forecasts has the potential to improve our understanding of the trigger mechanisms leading to CI.

The main motivation for this study was to increase understanding of the processes leading to CI in weakly forced environments through application of object-based CI composites commonly used in CI satellite nowcasting studies. Application of the satellite-based techniques provides a novel method to evaluate high-resolution models using established satellite-based metrics. NWP models allow in-cloud processes to be resolved, but as NWP resolution has increased the representation of CI location and timing has thus far shown limited improvement (Kain et al. 2008; Schwartz et al. 2009; Langhans et al. 2013; Burghardt et al. 2014). Evaluating model performance using standard point-by-point methods is difficult at higher resolutions because small positioning errors in the forecast may be penalized for not forecasting the event at the

observation point even though qualitatively it may be a better forecast. Improvements in CI forecasting have been demonstrated when assimilating surface observations (Liu and Xue 2008; Sobash and Stensrud 2015); however, forecasting on the meso–α storm scale (2.5-25 km) requires a high-density network of surface (Madaus and Hakim 2016, 2017) or satellite observations (e.g. Yussouf et al. 2016; Zhang et al. 2019; Jones et al. 2020). Further, forecasts from model simulations can drastically change in relation to the assumptions in the model setup (e.g. Otkin and Greenwald 2008; Cintineo et al. 2014; Griffin et al. 2017), and the accuracy of storm location and timing remains an issue (Weisman at al. 2008; Mittermaier at al. 2013; Shrestha at al. 2013; Bytheway and Kummerow 2015, 2018). Because satellite and radar observations alone are unable to fully resolve CI, additional insight concerning processes occurring within the cloud are needed to improve forecast accuracy. This can be accomplished using high-resolution NWP simulations that provide information about in-cloud microphysical processes. In order to apply knowledge gained from simulated cloud properties to observations, however, we must ensure that the forecasted cloud properties are representative of the convection reaching CI. Convection produced in weakly forced environments, that commonly occur in the Southeastern United States, therefore provides the opportunity to evaluate CI processes driven largely by cloud microphysics in conditions devoid of large synoptic forcing.

Linking output from NWP models to geostationary satellite observations has been accomplished by previous studies through the use of radiative transfer models to simulate satellite BTs (e.g. Tselioudis and Jakob 2002; Lopez et al. 2003; Grasso and Greenwald, 2004; Otkin and Greenwald 2008; Otkin et al. 2009; Cintineo et al. 2014; Lee et al. 2014; Thompson et al. 2016; Griffin et al; 2017; Bytheway et al. 2017; Griffin et al. 2020; Kim et al. 2020). These

studies track and compare mean characteristics of clouds as a whole, yet lack an ability to evaluate cloud morphology. Work is therefore needed in order to track specific processes driving individual convective cells evolving from shallow cumulus to clouds that deepen and produce heavy precipitation within an environment with little to no mesoscale or synoptic-scale variability. Comparing the observed and simulated BTs can be challenging due to timing and location errors in the forecast cloud objects, which makes point-to-point comparisons with traditional verification methods difficult (Griffin et al. 2017). Object-based analysis can improve these comparisons by accounting for spatial displacement errors (e.g. Burghardt et al. 2014; Griffin et al. 2017; Bytheway and Kummerow 2018). This study will build upon prior work that has primarily focused on larger cloud systems by examining the evolution of individual convective cells in a weakly forced environment.

The high-temporal resolution data from the *GOES-16* Advanced Baseline Imager (ABI; Schmit et al. 2017) provides an ideal dataset to track the life cycle of convection because the temporal resolution of 1-5 mins is more in line with the timescales of cumulus cloud growth (Gravelle et al. 2016). For this study, individual convective cells produced by high-resolution Weather Research and Forecasting (WRF) model simulations will be tracked and evaluated using geostationary-derived CI interest fields to understand how bulk microphysical parameterization schemes represent the formation and development of hydrometeor species, cloud growth, and precipitation processes. We present a strategy to evaluate the evolution of simulated convection using recent observation-based tracking techniques in parallel with recent methods used to describe CI in observational-based studies (e.g., Harris et al. 2010; Mecikalski et al. 2011; Mecikalski et al. 2016; Senf and Deneke, 2017). Mecikalski et al. (2011) demonstrated that

satellite BT CI interest fields describing cloud growth are most beneficial when nowcasting CI using geostationary satellites, specifically using Meteosat Second Generation data, which mimics those from *GOES-16*. These CI interest fields will be computed using *GOES-16* ABI observed and simulated model BT imagery, and then compared in lag-based composites of cloud objects as a function of the timing of CI. This composite-based method focuses the evaluation on the model ability to simulate the evolution of convection independent of the cloud location and time. The evaluation will also be applied to gain greater understanding of the cloud processes occurring within the clouds that lead to various cloud-top signatures depicted in satellite infrared (IR) imagery. Going forward, the paper is structured as follows: The case analysis, model setup, and observational data are described in Section 2, and the cloud tracking technique and methods are described in Section 3; analysis of the WRF simulations and discussion of the results are shown in Section 4, with a summary of the overall findings provided in Section 5.

2. Data and Model Setup

a) Geostationary data

This analysis will employ observations from the *GOES-16* ABI sensor (Schmit et al. 2017). Individual and combinations of ABI bands will be assessed that together provide a detailed depiction of the cloud properties in different parts of the troposphere (Fig. 2 in Schmit et al. 2017). The ABI IR BTs from spectral window regions are highly sensitive to cloud particles in the uppermost portion of a cloud and therefore provide valuable information about the horizontal and vertical extent of the clouds. The emphasis on IR channels in this work ensures continuous day–night cloud observations. The 2 km resolution IR channels on the ABI sensor also allow for

a more accurate discrimination of liquid and ice clouds that are crucial to evaluate the various mixed-phase and ice processes in a bulk microphysics parameterization scheme, as found by Mecikalski et al. (2010), Mecikalski et al. (2015) and Senf and Deneke (2017). BT-derived forecast factors used in this study include the evolution in cloud-top height (10.35 μm channel), cloud growth tendencies (10.35 μm BT tendency every 5 mins), and channel differences providing cloud-top glaciation estimates (8.4–10.35 μm BT difference). These *GOES-16* ABI channels are available over CONUS every 5 mins, which permits more frequent comparisons with the WRF output compared to previous satellite sensors. This in turn supports a more detailed comparison of clouds evolving in CI events, particularly the early stages of convection that may have been missed previously due to limited temporal resolution (Mecikalski et al. 2008).

b) Ground radar data

Ground-based NEXRAD S-band radar data for three radar sites located in Alabama and Mississippi (KBMX-Birmingham, KGWX-Columbus, and KDGX-Jackson) are used in this analysis. The spatial coverage of these radars is shown by the blue circles in Fig. 1. The NEXRAD data comes from Doppler weather radars that operate at S-band (10 cm) and Level 2 data is collected for the vertically resolved radar reflectivity. Volume scan data for the three radar sites are converted to a 1 km horizontal and vertical cartesian grid using the open-source Python Atmospheric Radiation Measurement Radar Toolkit (Helmus and Collis, 2016). Composite reflectivity data are created from the gridded data using the maximum reflectivity at each grid point and then the four closest reflectivity data points are matched to the closest 2 km

192 *GOES-16* IR observation. Radar scanning intervals are not constant due to changes in radar
193 volume coverage for a particular scan; therefore, we collocate the radar data to the nearest 5 min
194 *GOES-16* observations. Application of the radar reflectivities to CI identification is described in
195 Section 3.
196
197 *c) WRF model setup and simulated brightness temperatures*
198 The WRF-ARW model (version 3.9.1.1) is used to simulate a case study from 20 May 2018
199 that was characterized by weakly-forced deep convection across Alabama and Mississippi during
200 the afternoon and evening. A ridge over the domain brought a typical summer weather pattern to
201 the Mississippi and Alabama region that is devoid of major synoptic forcing mechanisms and
202 wind shear, yet with moderate afternoon instability. High pressure located off the eastern coast of
203 the United States provided the region with abundant moisture from the Gulf of Mexico. The
204 0000 UTC 21 May BMX sounding (not shown) indicates a freezing level near 4000 m and a
205 warm layer near 5800 m. CAPE was above 1500 Jkg^{-1} and surface temperatures exceeded 90 °F,
206 but moderate convective inhibition is observed with CIN near –40 Jkg^{-1}. Convection able to
207 surpass this warm lid would be able to grow towards deep convection across the entire region
208 during the afternoon and evening hours. Multiple slow-moving isolated convective cells with
209 damaging wind gusts and hail occurred across the region according to storm reports from the
210 Storm Prediction Center. Slow-moving convective features such as these are common in late
211 spring and summer across this region and allow for easier tracking with satellite and radar
212 observations. To capture the fine-scale convective features associated with this event, three two-
213 way feedback permitted WRF model domains are used with nests possessing 12.5 km, 2.5 km,

214 and 500 m resolution, respectively, centered over Alabama and Mississippi (Fig. 1). The initial
215 and lateral boundary conditions are provided every 6 h by the National Center for Environmental
216 Prediction final (NCEP FNL) analyses on a 0.25° latitude/longitude grid. The WRF model
217 simulations contain 53 sigma levels, with the model top set to 25 hPa.

218 Three commonly used bulk microphysics schemes are examined in this study: the Thompson
219 et al. (2008), Morrison (Morrison et al. 2005, 2009), and WRF double-moment 6-class (WDM6;
220 Lim and Hong, 2010) schemes. All of these microphysics schemes predict mass mixing ratios of
221 cloud water, rainwater, cloud ice, snow, and graupel. The Thompson and WDM6 are mixed-
222 moment schemes, where WDM6 predicts two-moments (mixing ratio and number concentration)
223 in warm rain processes and the Thompson scheme predicts two-moments of cloud water and ice.
224 The two-moment Morrison scheme predicts mixing ratios for all cloud hydrometeor categories
225 and number concentrations are also predicted for cloud ice, snow, rain, and graupel. Each
226 microphysics scheme allows output of a radar reflectivity factor based on the Rayleigh
227 approximation, which is very similar to the S-band wavelength observations of our ground-based
228 radar data.

229 All WRF simulations use an identical model configuration, apart from the microphysics
230 scheme. Simulations are initialized at 1200 UTC, which allows sufficient model spin-up as the
231 first CI case occurs near 1700 UTC. Physics options included are the Rapid Radiative Transfer
232 Model for Global Climate Models (RRTMG; Iacono et al. 2008), the nonlocal-mixing Yonsei
233 University (YSU; Hong et al. 2006; Hong 2010) planetary boundary layer scheme, and the Noah-
234 MP land surface model (Niu et al. 2011). No cumulus parameterization is used on the higher

resolution 2.5 km and 500 m domains, whereas the Tiedtke (Tiedtke 1989; Zhang et al. 2011) scheme is used on the outermost 12.5 km domain.

The evolution of CI events will be assessed on the high-resolution 500 m innermost domain. Data were output every 5 mins to be consistent with the temporal resolution of CONUS *GOES-16* ABI data. Following Griffin et al. (2017), the Community Radiative Transfer Model version 2.1 (CRTM; Ding et al. 2011) was used to convert the WRF model output into simulated *GOES-16* ABI IR BT data. The CRTM provides all-sky top-of-atmosphere BTs that incorporate the *GOES-16* viewing geometry for channels 7-16 of the ABI (3.9–13.3 μm). Top-of-atmosphere BTs in clear-sky scenes are generated using surface emissivity provided by the University of Wisconsin High Spectral Resolution Emissivity Algorithm (Borbas et al. 2007), and WRF model predicted surface skin temperature, 10-m wind speed, and vertical profiles of temperature, pressure, and water vapor mixing ratio. Cloudy scenes use the above information, as well as derived cloud properties (i.e. effective particle radius, cloud water content) consistent with the assumptions made by each cloud microphysics parameterization scheme used (e.g. Otkin et al. 2007; Thompson et al. 2016; Griffin et al. 2017). Cloud properties were derived individually for each cloud species and input into the CRTM to compute the cloud optical properties (i.e. single scatter albedo, asymmetry parameter, and full scattering phase function) for each model grid point and vertical layer. Finally, the combined set of hydrometeor optical properties were used to compute the top-of-atmosphere BT data for each IR band measured by the ABI.

3. Cloud object identification and CI compositing

a) Cloud object and CI identification

Cloud tracking and detection methods are applied identically for the observed and simulated BT datasets. Cloud tracking is based on 10.35 μm BTs because radar observations may not be available during the entire cloud lifecycle (Mecikalski et al. 2006). Cloud objects are identified based on the Tracking Of Organized Convection Algorithm through 3-D segmentation (TOOCAN; Fiolleau and Roca, 2013) algorithm and tracked through time when overlapping areas occur in successive images of cloud objects (e.g. Vila et al. 2008). This tracking scheme takes advantage of the fact that IR BTs are sensitive to cloud particles (their size, phase, and amount) in the upper portion of the cloud giving extensive information on the horizontal and vertical extents of cloud tops, which helps separate cloud clusters through time. Using this iterative method of tracking clouds using the IR channels has been shown to be effective tracking intense convection (e.g. Wall and Hartmann 2018; Cancelada et al. 2020).

To maintain consistency with the ABI observations, model gridded BTs are averaged to 2-km grid spacing when identifying objects. Inspection of the BT imagery showed that the coldest cloud tops during the observation period have BT < 210 K. Thus, cloud boundaries are first searched for using BT < 210 K and then iteratively increasing by 2.5 K to detect cloud boundaries (Fig. 2), where the warmest cloud boundaries within this case study are defined as where the 10.35 μm BTs are < 285 K. This warm cloud boundary threshold helps capture cloud growth before CI is detected, but also ensures that possible surface BT contamination is excluded. Fiolleau and Roca (2013) describe the cloud detection as iteratively growing cloud "seeds" from colder to warmer BTs. In this work, clouds are identified using the TOOCAN methodology by detecting initial boundaries using a low BT threshold of 210 K. For each identified object, pixels are added to the cold cloud top object using a 2.5 K warmer BT

279 threshold to identify the edge of the new boundary. The warmer BT threshold is also applied to
280 detect new cloud object "seeds". This iterative process of extending the cloud boundary by 2.5 K
281 is repeated until each of the grid boxes within a cloud object are colder than 285 K or if cloud
282 overlap is detected with a neighboring object. Once cloud objects are identified for each 5-min
283 timestep from the observations and simulations, the SciPy data package (Virtanen et al. 2020) is
284 used to detect and track the cloud object overlap between timesteps. To be consistent with
285 previous observational studies (e.g. Roberts and Rutledge 2003; Mecikalski et at 2006;
286 Weckwerth and Parsons 2006), a cloud object from the *GOES-16* ABI and WRF simulations will
287 be defined as CI when radar reflectivity > 35 dB*Z* occurs in a cloud object. This threshold is
288 common in thunderstorm nowcasting studies where CI is exclusively defined using a radar
289 precipitation echo intensity criteria of ≥30–40 dB*Z* (Browning and Atlas 1965; Marshall and
290 Radhakant 1978; Schreiber 1986; Wilson and Schreiber 1986; Wilson et al. 1992; Wilson and
291 Mueller 1993; Mueller et al. 2003; Walker et al 2012; Lee et al. 2016; Han et al. 2019). The 35
292 dB*Z* threshold signifies convective precipitation near the surface of ~8 mm h^{-1}. Clouds reaching
293 this threshold typically produce significant precipitation, but it does not guarantee that the CI
294 events will lead to long-lived convective storms (Mecikalski et al. 2015). To mitigate vertical
295 resolution differences between NEXRAD and the model vertical grid we define CI when the
296 maximum reflectivity in the cloud column exceeds 35 dB*Z* (e.g. Matthee et al. 2014; Senf and
297 Deneke, 2017).
298
299 *b) Composite analysis methodology*

300 Several physical cloud characteristics from observed and simulated cloud objects reaching CI
301 are tracked and compared using lag-composite analysis. When the radar reflectivity within a
302 cloud object surpasses the 35 dB*Z* threshold, that timestep is labeled time lag zero and the data
303 before, during, and after this CI timestep are composited to describe the evolution of the cloud
304 objects. Objects reaching CI are examined and compared when the cloud persists longer than 35
305 mins to track the cloud evolution 15 mins before and 15 mins after the 5-min period in which CI
306 is detected. Composited data includes the CI forecast interest fields described in Section 2a,
307 cloud area (defined using the number of grid boxes in the cloud object), and model-based
308 properties from profiles of mixing ratios for each of the hydrometer types. After cloud objects
309 are identified for each time lag, the cloud characteristics and CI forecast interest fields are
310 derived. For *GOES-16* ABI data, the BT interest fields described in Section 2.1 are derived using
311 the grid boxes containing the two coldest 10.35 μm BTs within the cloud object (e.g. Mecikalski
312 et al. 2010). For the WRF simulations, the coldest two grid boxes that were averaged to 2 km
313 within each cloud object are used to derive the CI forecast interest fields, which is 32 grid boxes
314 at 500 m grid spacing. If cloud objects are smaller than the grid boxes required for averaging the
315 observed or modeled cloud objects, then all cloudy grid boxes are used with the cloud object
316 boundaries.

317 **4. Results**

318 *a) Comparison of domain-based characteristics*

319 Cloud objects are compared over a 3-hour period beginning at 1700 UTC, which is near the
320 time the first CI object was observed in *GOES-16*. Table 1 provides a summary of the total cloud
321 objects and CI cases tracked, and the time of first CI occurrence. This 3-hour period is chosen to

provide a sufficient number of objects, but also to limit new CI events that originate under larger cloud anvil regions where passive satellite observations cannot accurately discriminate multi-layer cloud structures (Mace and Wrenn 2013). Model and observed cloud objects are first compared using domain-wide statistics to understand the characteristics of the cloud objects without considering the stage of the cloud lifecycle. The first observed *GOES-16* CI event occurs at 1655 UTC, with the first CI occurring at 1645 UTC, 1640 UTC, and 1700 UTC for the Thompson, Morrison, and WDM6 schemes, respectively. Overall, the Thompson and Morrison schemes produce more CI objects than was observed in *GOES-16* data, whereas the WDM6 simulation more accurately represents the number of observed CI objects.

CI cases over the 3-hour period and their occurrence, fractional coverage, and cloud object areas are illustrated in Fig. 3. In Fig. 3a and Fig. 3b the number of CI cases that are active at each timestep are represented by the solid lines and in Fig. 3c the range of CI cloud object areas are represented by the box-and-whisker diagrams. The data are plotted at 15-min intervals starting at 1700 UTC. The number of CI cases in the Morrison scheme quickly increases 30 mins after the start of the observation period; however, the WDM6 scheme has a delay in occurrence compared to the other simulations and observations. Overall, the observations and simulations show an increase in cloud object area over time. When compared to the observations (grey bars) the ranges in active CI cloud sizes from the simulations display a general agreement in median cloud object area throughout the three-hour period where the ranges in object size are close to the *GOES-16* observations.

The fractional coverage of active cloud objects (Fig. 3b) is similar to the pattern of CI occurrence (Fig. 3a) for each configuration, with the Thompson and Morrison schemes

344 producing more objects covering a larger fractional than the WDM6 scheme. From 1700 UTC to
345 around 1900 UTC, the Thompson and Morrison cloud object size interquartile range (IQR)
346 shown in Fig. 3c is similar to observations, but the simulations contain more active cloud objects
347 leading to a higher fraction of domain coverage (Fig. 3b). As clouds get larger towards the end of
348 the observed period the fractional coverage for all simulations merge towards the observations,
349 but the Morrison simulation contains more objects (Fig. 3a) and the Thompson cloud object size
350 IQR is smaller than indicated by the *GOES-16* observations at 1945 UTC (Fig 3c). This suggests
351 that the Thompson and Morrison simulations produce too many small cloud objects compared to
352 observations. The WDM6 simulation has a delay in occurrence, which leads to a lower fractional
353 coverage throughout most of the observed period (Fig 3b). The WDM6 simulation contains a
354 higher cloud object size IQR starting around 1800 UTC, where CI cloud growth becomes more
355 rapid than the other two microphysics schemes and cloud object occurrence and fractional
356 coverage begins to move closer to the *GOES-16* observations. Further insight into microphysical
357 reasonings leading to this delay in CI development for the WDM6 scheme will be provided in
358 Section 4b.

359 To investigate how the cloud height evolves within the cloud objects, Fig. 4 displays
360 normalized frequency distributions of 10.35 μm BT for four different times in the WRF forecasts
361 for all objects in a timestep. Figure 5 shows the 10.35 μm BTs at 1900 UTC for the observations
362 and model simulations. Inspection of Fig. 4 shows that there is a shift from shallow convection at
363 1700 UTC (mostly warmer BTs) towards a mix of shallow, congestus, and deep convection from
364 1800–1900 UTC (higher percentage of colder BTs), and predominantly deep convection with
365 anvil regions at 2000 UTC. In the Morrison simulation, a higher fraction of convection occurs at

366 1800 UTC for BT near 260 K, whereas the WDM6 and Thompson schemes simulate a higher
367 fraction of cloud tops colder than what was observed by the *GOES-16* ABI. Quantitively, this
368 bias is found in the coldest cloud objects, which are compared using the coldest 10^{th} percentile of
369 10.35 μm BT (Table 2) derived using a cumulative distribution function sorted by cloud-top
370 temperature. Cold biases are largest in the Morrison scheme at 1700 UTC and continue through
371 1800 UTC. Starting at 1800 UTC evidence of a cold bias from deeper convection is found in the
372 Thompson scheme and becomes more pronounced at 1900 UTC where BT < 240K are more
373 frequent. This bias pattern continues to the 2000 UTC timestep. Griffin et al. (2017) found
374 similar behavior when assessing output from the High-Resolution Rapid Refresh model.
375
376 *b) Composite-based evaluation of CI*
377 The differences in Figs. 3 and 4 begin to scratch the surface on possible organizational
378 differences in the spatial cloud coverage between the observations and microphysical schemes.
379 Previous studies have investigated cloud-top BT biases through matching cloud objects spatially
380 and temporally to verify CI forecasts (e.g. Burghardt et al. 2014) or by implementing object-
381 based analysis to track cloud systems to assess characteristics beyond point-by-point analysis
382 (e.g. Griffin et al. 2017). However, these evaluations lack validation of the model representation
383 of the cloud evolution characteristics leading to CI itself. The differences in Fig. 3 illustrate a
384 direct overestimate of CI frequency during the model forecasts, but it is difficult to distinguish
385 the mechanisms leading to this from domain-based or system-based statistics alone. Evaluation
386 of CI processes based on the cloud life cycle is possible using composite strategies and allows
387 investigation of simulated CI characteristics without the need to match with the observations in

388 space and time. While this does not provide the same dichotomous validation when model
389 objects are matched with observations in space and time, it allows evaluation of the full breadth
390 of CI characteristics exhibited by the simulations.

391 To understand how clouds leading to CI evolve through time, the evolution of three satellite-
392 based cloud-top interest fields will be described to characterize the changes in cloud-top growth
393 and microphysical state. The 5-min temporal information content from the ABI sensor provides
394 the opportunity for observing growth closer to cloud scales (e.g., Gravelle et al. 2016; Senf and
395 Deneke, 2017) when evaluating the model simulations. The satellite-based interest fields are
396 derived using three BT-based methods that represent the cloud-top height using the 10.35 μm
397 BT, 10.35 μm BTs cloud growth tendency at 5-min intervals, and cloud-top glaciation using 8.4
398 μm–10.35 μm BT differences. Figures 6 and 7 provide box and whisker plots for cloud growth
399 CI interest fields that detail the distribution of cloud-top BTs for timesteps 15 mins before and
400 after CI is observed (time lag = 0 at CI).

401 Similar to clouds observed in Mecikalski et al. (2013), the 10.35 μm BTs begin near 270 K
402 15 min before CI occurs and continually cool (grow vertically) throughout the period (Fig. 6).
403 For the Thompson and Morrison schemes, clouds 15 mins before CI are warmer (shallower)
404 compared to the ABI observed ranges. The median BTs from the Thompson and Morrison
405 schemes move towards the *GOES-16* ABI median values over time resulting in increased cooling
406 rates before CI occurrence (Fig. 7). In Fig. 7, the growth rates exhibit similar characteristics to
407 the 5-min analysis in Senf and Deneke (2017), where the maximum cooling rates occur near CI
408 and then the cloud top cooling rate decreases afterwards. The Morrison scheme displays faster
409 growth rates 10 to 15 min before CI and the Thompson scheme exhibit a larger increase in cloud

410 growth 5-mins before CI. Further, all of the WRF model simulations exhibit large ranges in BTs
411 compared to the observed ABI clouds particularly after CI occurs. The model simulations
412 produce a higher fraction of clouds that begin to warm, or slow in growth, after CI is detected
413 (Fig. 7), suggesting cloud growth has ceased. When tracking the clouds through time, the CI
414 cases from the Morrison simulation last no more than 20 min 42% of the time after CI was
415 detected, whereas 35% of the CI cases in the Thompson simulation last 20 min or less, which
416 suggests a higher number of congestus clouds compared to longer-lived deep cumulonimbus
417 clouds in the Thompson and Morrison simulations. Mean values for the observed and simulated
418 values are shown in Table 3 using the IQR, defined as the 25–75% quartiles of the data in Figs. 6
419 and 7. The differences described above are also evident in Table 3, where higher growth rates
420 before CI and a switch towards positive (warming) after CI are found in the Thompson and
421 Morrison schemes.
422 There is a clear disconnect in the cloud development in the WDM6 microphysics that leads
423 to a delay in CI detection resulting in colder cloud tops (Fig. 6; light green bars). While the
424 WDM6 cloud growth rates in Fig. 7 exhibit a similar pattern as the Thompson and Morrison
425 schemes, cloud heights in Fig. 6 are higher (colder), demonstrating that CI is detected later in the
426 cloud life cycle compared to the other simulations. To further investigate cloud growth in the
427 WDM6 simulation, the cloud evolution is plotted starting an additional 30 min before CI was
428 detected (hatched bars in Figs. 6 and 7), which is the timestep the median WDM6 10.35 μm BTs
429 best match the ABI observations. The 30-min lagged WDM6 10.35 μm BTs in Fig. 6 more
430 closely resemble the ABI observations, but the growth rates in Fig. 7 no longer exhibit the
431 maximum cooling at timestep zero originally found in both the *GOES-16* observations and

simulated clouds. Instead, the lagged WDM6 evolution is more linear. The WDM6 scheme typically produces rain drop sizes that are too small (Morrison et al. 2015; Johnson et al. 2016; Lei et al. 2020). Radar reflectivity is proportional to the sum of the sixth power of the diameter; therefore, smaller drop size distributions will lead to lower reflectivities in the growing convection. Further, previous research describes the need for a glaciation-driven latent heat boost within clouds to elevate them towards CI (e.g., Zipser 2003; Mecikalski et al. 2016; Senf and Deneke, 2017). The results from the cloud-top BTs indicate that the WDM6 scheme likely has a lag in rain growth and cloud glaciation that produces the added mid-tropospheric latent heating needed to reach CI, and subsequent large enough hydrometeors to produce a radar echo greater than 35 dB*Z*.

Direct comparison of BT channels sensitive to cloud top microphysical changes and glaciation help shed light on how accurately the microphysics schemes handle ice processes in the top levels of the cloud (e.g. Mecikalski et al. 2010; Senf and Deneke 2017). Figure 8 displays box and whisker plots for the observed and simulated 8.4 μm–10.35 μm BT differences. Due to the different optical properties between liquid and ice, the BT difference switches from negative (below –2 K) for optically thick liquid clouds towards positive when the cloud top becomes fully glaciated (Baum et al. 2000). The observed BT difference from *GOES-16* shows that the clouds start as fully liquid 15 min before CI and then the BT difference trends towards less negative values thereafter, plateauing near –1 K. Baum et al. (2000) describe how positive trends in this BT difference field are driven by the presence of larger ice and liquid particles at cloud top. The larger particle size leads to smaller BT differences, and suggests that a mixed

phase state is possible at cloud top in the *GOES-16* observations after CI is detected. Some clouds do exhibit positive BT differences; however, they are beyond the box and whisker ranges.

The three WRF bulk microphysical schemes are characterized by different evolutions of cloud-top glaciation BT differences (Fig. 8). The Thompson scheme has the closest pattern to observations with clouds starting around –2 K 15 mins before CI and converging to a BT difference near –0.5 K at CI. The majority of cloud tops contain a negative BT difference in the Thompson simulation with a few switching to positive 15-mins after CI detection. The Morrison scheme more efficiently converts from liquid to ice phases, and the glaciation trend increases monotonically before and after CI. Cloud-top glaciation is found in clouds starting at time-lag zero and the amount of cloud tops with positive BT differences increases monotonically until the majority of clouds are glaciated 15 min after CI. Similar to the observations and the Thompson scheme, the WDM6 simulation BT differences plateau after CI, but due to the delay in CI detection, clouds exhibit ice glaciation before CI detection. Using the 30-min lagged WDM6 BTs described above, the glaciation BT differences resemble the Thompson and observed *GOES-16* trend but continues to grow linearly. The presence of ice likely demonstrates that larger liquid precipitation hydrometeors are absent in the early WDM6 development, thereby delaying the detection of CI.

To examine differences in the evolution of in-cloud microphysics, Fig. 9 presents vertical profiles of liquid and frozen cloud mixing ratios for each simulation from 5 min before until 10 min after CI is detected. To provide additional insight into the behavior of the WDM6 scheme, the bottom row shows vertical profiles for the cloud mixing ratios from 25 to 10 min preceding CI. For all of the microphysics schemes, CI detection is coincident with the emergence of a

475 precipitating core near 4–5 km and the formation of graupel near the cloud top. The WDM6
476 simulation contains a similar rain mixing ratio profile 5 min before CI when compared to the
477 Thompson and Morrison simulations. In the WDM6 simulation, the delay in CI detection leads
478 to more cloud water lofted to the upper levels along with higher mixing ratios for frozen
479 hydrometers. For WDM6, the emergence of rain mixing ratios does not occur until 10 mins
480 before CI detection. Starting 25 min before CI cloud mixing ratios are still located well above the
481 freezing level. Near 15 min before CI, small amounts of cloud ice and snow occur before the
482 emergence of rain in the WDM6 simulation and the cloud continues to grow with cloud mixing
483 ratios located as high as 10 km above the surface. This is consistent with the large cold biases in
484 10.35 μm BTs in Fig. 6 and Table 3. Both the WDM6 and Morrison schemes produce larger
485 amounts of graupel and snow after CI leading to the positive BT difference bias shown in Fig. 8.
486 The Thompson scheme still produces graupel in the upper levels of the cloud but is more
487 efficient at producing rain at the surface. This leads to less ice aloft and the development of a
488 plateau in the 8.4–10.35 μm BT differences after CI in the Thompson simulation and *GOES-16*
489 observations; the 8.4–10.35 μm BT differences plateau in the Thompson simulation centered on
490 –1, verifying the lack of cloud-top glaciation.
491
492 *c) CI processes related to cloud growth*
493 The WRF simulations contain more CI cloud objects than observed, where the Thompson
494 and Morrison simulations have the most cloud objects reaching CI. As shown in Fig. 7, after CI
495 is detected, the simulated clouds have a large spread in growth rates. The *GOES-16* observed BT
496 histograms presented in Fig. 4 are characterized by 10.35 μm BT peaks near 260 K and 220 K

497 signifying that the CI cloud objects are subset into shallower precipitating congestus clouds with
498 warmer cloud tops and clouds that continue to grow into deep cumulonimbus clouds. The 35
499 dBZ threshold used to define CI in this case study captures precipitating clouds within the 10.35
500 μm 260 K and 220 K cloud subsets. These clouds all reach CI and likely produce significant
501 precipitation; however, combining the two subsets of cloud growth can lead to ambiguity when
502 comparing the model and observational differences.

503 To investigate the cloud characteristics associated with the varying life cycles of cloud
504 growth, the CI definition is modified to discriminate both sets of clouds. The cloud evaluation
505 will partition CI cloud objects into those reaching 10.35 μm BTs < 250 K at some point in their
506 lifecycle and those with cloud-top BTs remaining warmer than 250 K. The 250 K threshold was
507 chosen using the BT histograms in Fig. 4, and since the clouds observed by *GOES-16* reaching
508 250 K demonstrate continuous growth after CI. For convenience, we will refer to cloud objects
509 reaching the 250 K threshold as the "cold-CI cloud" category and cloud objects remaining
510 warmer than 250 K as the "warm-CI cloud" category. The 250 K threshold will be applied to the
511 observed and simulated CI cloud objects. The warm- and cold-CI clouds from the WRF
512 simulations will be further subset by the top 50% of cloud objects in each category that most
513 closely match the observed *GOES-16* observed growth rates after CI is detected. Cloud objects
514 outside the top 50% best matching *GOES-16* growth rates illustrate simulated cloud objects
515 where growth is outside the ranges measured by the *GOES-16* observations. Because the
516 temporal delay for CI events in the WDM6 simulation leads to a limited amount of cases where
517 cloud-top BTs remain warmer than 250 K, this analysis will focus on the Thompson and
518 Morrison simulations only.

519 Table 4 provides a summary of the total CI cloud objects tracked when CI clouds are
520 separated into warm-CI and cold-CI cloud cases. It is evident that the overestimation of
521 simulated cloud objects reaching 35 dBZ is due to an increase in warm-CI clouds with 21, 75,
522 and 84 warm-CI clouds from *GOES-16* observations, Thompson and Morrison, respectively. The
523 Thompson and Morrison schemes produce 46 and 54 cloud objects reaching 250 K, respectively.
524 Though this is still higher than the 31 objects observed by *GOES-16*, it does lead to a better
525 match than when using the 35 dBZ CI definition alone.
526 The resulting 10.35 μm cloud-top BTs and BT growth rate tendencies using the warm- and
527 cold-CI cloud categories are displayed in Figs. 10 and 11. Separating the CI cloud objects into
528 warm and cold categories leads to a clear difference in the 10.35 μm cloud-top heights in Fig. 10.
529 Near the time CI is detected, the observed and simulated warm-CI cloud growth halts and the
530 10.35 μm BTs remain nearly constant (Fig. 10a). This is consistent with the warm-CI clouds BT
531 tendency where most clouds observed by *GOES-16* display zero tendency and both sets of
532 simulations warm after CI detection resulting in positive BT tendencies (Fig 11a). On the other
533 hand, there is a clear deepening in the cold-CI clouds after CI as the 10.35 μm BT continues to
534 decrease (Fig. 10b). The cloud-top BTs for cold-CI clouds are well below the freezing level of
535 273 K at the time CI is detected. The cloud-top BTs in Fig. 10 and tendencies in Fig. 11 for the
536 cold-CI cases resemble cloud-top BT trends described in Matthee and Mecikalski (2013) who
537 demonstrated that rapidly growing convection (growth rates ~10°C/15 mins) are more likely to
538 produce heavy rain and lightning compared to CI cases with slower growth.
539 Comparing the top 50% of simulated cloud objects most closely matching the observed
540 *GOES-16* growth rates for warm and cold-CI clouds naturally leads to improvement for both

cloud height and growth rates within the best matched cases. For these clouds, median cloud growth rates become closer to observations and the spread in 10.35 μm BT and BT growth rates (Fig. 10c-d and Fig. 11c-d) after CI detection are greatly reduced. The 10.35 μm cloud-top BTs in the simulations remain consistently warmer than *GOES-16* before CI detection leading to the same pattern of increased growth rates for Thompson cloud objects shown previously in Fig. 7. The Morrison cloud objects display increased growth rates 10 min before CI in the warm-CI cases in Fig. 11a, but growth rates closer to *GOES-16* occur afterwards. The simulated warm-CI cloud cases outside the top 50% best matching *GOES-16* observed growth in Fig. 10e and Fig. 11e show signs of decay quickly after CI is detected where cloud growth trends are warmer than the observations, whereas the simulated cold-CI cloud cases in Fig. 10f and Fig. 11f display rapid growth at CI detection and 5-min after CI. It is interesting to note that the warm-CI cloud objects contain cloud growth rates that are similar to the cold-CI clouds before and at CI detection. This suggests that in the early stages of CI, the BT interest fields used to forecast CI might not be able to differentiate clouds with sustained growth from those that decay. This scenario could lead to false positives in geostationary satellite-based severe storm nowcasting algorithms since early cumulus cloud growth signatures are not always associated with CI events in the coming 30-45 min (Mecikalski and Bedka 2006).

Figure 12 uses 8.4 μm–10.35 μm BT differences to evaluate signals in cloud-top glaciation in the warm-CI and cold-CI cloud categories. For warm-CI clouds, the WRF simulated BT differences closely track the observations, where the clouds start as fully liquid 15 min before CI and then the BT difference trends towards less negative values thereafter, plateauing just above –2 K. For the cold-CI clouds, the *GOES-16* observed BT difference are closer to zero; however,

563 negative values before and after CI indicate a cloud top that is not fully glaciated. A slight
564 positive trend occurs in observed cold-CI cloud BT differences proving evidence that cloud-top
565 microphysics contain larger hydrometeor sizes or ice after CI, which does not occur in warm-CI
566 clouds. A larger number of outliers occur above zero for the observations and simulations
567 indicating that more clouds have reached a fully glaciated state in the cold-CI category. For both
568 microphysics schemes, the simulated cloud BT differences are nearly constant until 5 min before
569 CI, thereby demonstrating a possible delay in the presence of ice or larger liquid hydrometeors
570 near the cloud top compared to observations. At CI detection, BT differences for both
571 microphysics schemes begin to quickly move toward more positive values and display evidence
572 of a glaciated cloud top 15 min after CI. This positive BT difference also exists in the Morrison
573 scheme for warm-CI clouds, providing further evidence of an overestimation of cloud ice after
574 CI.

575 Figure 13 compares mean mixing ratio profiles for the warm- and cold-CI cloud categories.
576 Differences are evident at the time when CI is detected, where the Thompson scheme more
577 efficiently produces rain hydrometeors than the Morrison scheme. There is also a discernable
578 difference between the warm-CI and cold-CI clouds, where mixing ratios from the cold-CI
579 clouds are consistently larger than occurred during the warm-CI cloud objects. For example,
580 profile maxima in cloud water mixing ratios remain higher in the cold-CI clouds. This sustained
581 cloud water source likely aids the creation of rain, graupel, and other ice hydrometeors, but it is
582 difficult to fully evaluate how the mixing ratios are impacting growth due to the differences in
583 mixing ratios between the microphysics schemes.

584 Figure 14 displays cloud mixing ratio tendency profiles for cloud objects in the warm-CI and
585 cold-CI cloud categories. Cold-CI cloud objects are further separated into the best matched cloud
586 objects and cloud objects that experience more rapid growth described in Fig. 10. All warm-CI
587 cloud objects are combined as the tendency profiles are similar. The tendency profiles were
588 created by differencing each 5-min interval with the timestep before it for each cloud object and
589 then averaged. The tendency profiles exhibit better agreement between the microphysics
590 schemes and are able to describe how changes in cloud microphysics could impact the growth of
591 the cloud. The mixing ratio tendency profiles for the warm-CI and cold-CI cloud categories are
592 similar before CI is detected, particularly in the Thompson scheme. In Fig. 13, increases in rain
593 mixing ratios in the simulated clouds develop near 4 km in the time step before CI detection.
594 This increase of rain hydrometeors leads to CI detection five minutes later. Five minutes before
595 CI, there is an discernable difference in the cloud water fluxed from the lower-levels of the cloud
596 to the upper levels, where the best-matched and rapid-growth cold-CI clouds lose less cloud
597 water compared to the warm-CI clouds. Cloud water is gained near 4 km for the warm-CI clouds,
598 best-matched cold-CI clouds, and rapid-growth cold-CI clouds, but less cloud water is lost below
599 3 km where a smaller negative cloud water tendency occurs in cold-CI cloud categories. This
600 tendency occurs at the CI timestep as well.
601 At time-lag zero when CI is detected, both microphysics schemes show increases in rain
602 water mixing ratios throughout the depth of the cloud, which monotonically increases as a
603 function of growth and the development of graupel occurs between 6–8 km. Five minutes after
604 CI is detected, the sustained cloud water in the lower levels of the cloud leads to higher rain
605 mixing ratios and a monotonic increase in graupel from warm-CI clouds to the cold-CI clouds,

606 which is found in both of the microphysics schemes. This helps confirm previous geostationary-
607 based assessments (e.g. Mecikalski et. al. 2016a,b; Senf and Deneke, 2017) that suggest growth
608 related to CI is aided by latent heat release from ice formation near and below cloud top. Figure
609 13 also shows that the process requires sustained latent heating in the lower levels from
610 condensation, which was also shown to be the case when 1-min resolution *GOES-14* data were
611 used to analyzing cumulus clouds undergoing the CI process (Mecikalski et al. 2016b). For the
612 warm-CI clouds in Fig. 13, the larger loss of cloud water in the lower levels of the clouds leads
613 to lower rain and graupel mixing ratios with negative tendencies for all cloud species above 4 km
614 10 min after CI was detected. Thus, clouds lacking the sustained source of low-level cloud water
615 are unable to sustain their growth over time.
616 Due to the warm and moist boundary layer found in the southeastern United States the warm
617 (>0°C) portion of the cloud is 3–4 km deep (Fig. 9), and accurate representation of warm rain
618 processes are essential for CI in weakly forced environments over this region. Combined radar
619 and geostationary satellite studies have demonstrated that heavily raining convection with similar
620 glaciation BT differences found in Fig. 8 and Fig 12 typically contain weaker updrafts and lower
621 ice contents at the cloud top (e.g. Mecikalski et al. 2013; Matthee et al. 2014; Senf and Deneke;
622 2017) compared to lightning producing storms; therefore, warm rain processes are a likely
623 pathway to make a 35 dB*Z* echo for both the warm-CI clouds and cold-CI clouds. Early rain
624 formation dictated by the auto-conversion process varies between the microphysics schemes
625 resulting in the differences found in Fig. 13 and resulting ice aloft in the cloud (e.g. Bao et al.
626 2019). The ABI comparisons in Figs. 10 and 11 help demonstrate that the simulations can
627 replicate the evolution in CI BT signatures. The comparisons of the BT differences associated

628 with cloud phase provide evidence that the Morrison scheme produces too much graupel in the
629 best-matched cases (Fig. 14). While the Thompson scheme best matches the observed 8.4 μm–
630 10.35 μm BT difference for this case study for both warm- and cold-CI clouds, further evaluation
631 assessing the sensitivity of the CI processes with land surface models and planetary boundary
632 layer schemes will be needed.
633
634 **5. Discussion and Conclusions**
635 In this study, the characteristics of simulated convection leading to CI from different bulk
636 cloud microphysics schemes are assessed using version 3.9.1.1 of the WRF model. The study
637 examined the evolution of cloud objects associated with CI for a case study from 20 May 2018
638 where weakly forced convection occurred over parts of Mississippi and Alabama that eventually
639 lead to multiple reports of high wind and hail. Evaluating in this environment provides analysis
640 where microphysics are the primary driver in pushing convection towards heavily precipitating
641 convection. Three model sensitivity experiments employing 500-m horizontal grid spacing were
642 completed where all model components were identical except for the cloud microphysics
643 scheme. *GOES-16* ABI infrared BTs were simulated for each model experiment using the CRTM
644 and then directly compared to *GOES-16* observed BTs using a lag-composite analysis, where
645 time zero was defined as the time CI was detected. CI for the model and observations is defined
646 as the first time a 35 dBZ radar echo occurred in the cloud column. Three BT-derived fields
647 commonly used in CI nowcasting applications were compared between the models and
648 observations to understand changes in cloud-top height, cloud growth rate, and hydrometeor
649 phases over time.

650 In general, the WRF simulations were able to capture the general trend in cloud growth rates
651 and cloud top area over time when maximum cooling occurred near the time CI was detected.
652 The simulations contain a larger spread of 10.35 μm BTs after the detection of CI. Furthermore,
653 the amount of clouds reaching CI is too frequent in all simulations due to a large number of
654 convective cases reaching CI and then quickly decaying afterwards. This pattern was most
655 pronounced when using the Morrison scheme. For the Thompson scheme, around 35% of CI
656 cases sustain 20 mins or less after CI, whereas this increases to 42% in the Morrison scheme.
657 Too frequent convection could lead to issues when forecasting CI due to the prevalence of
658 convection formation in raining outflow boundaries in the southeastern United States (Goggins et
659 al. 2010). Delays in rain hydrometeor formation occur in the WDM6 bulk microphysics scheme,
660 which led to a delay in the detection of CI compared to the *GOES-16* observations. This then
661 caused a cold bias in the simulated 10.35 μm BTs > 20 K throughout the CI process when this
662 scheme was used. Lagging the WDM6 BT timeseries by 30 min improved comparisons with the
663 10.35 μm cloud-top BTs, but cloud growth rates no longer exhibited the maximum growth at CI,
664 likely due to the absence of ice growth at these timesteps and thus lacking the upper level latent
665 heating needed to support cloud growth.
666 Evaluating the simulated clouds using BTs demonstrates the benefits of using high-resolution
667 satellite observations to examine cloud processes using model simulations. It also provides a
668 platform to deconstruct cloud properties leading to trends in CI properties. When partitioning the
669 results into warm-CI and cold-CI clouds the simulated CI cases produce a range of 10.35 μm
670 cloud-top BTs more akin to the *GOES-16* observations. Although differences in microphysical
671 processes are evident, comparison of the tendencies in mixing ratio profiles from these two

microphysics schemes reveals agreement in the tendency of in-cloud mixing rations related to convection initiation and cloud growth. Cold-CI clouds are characterized by an increase in cloud water at lower levels near the time of CI that is then lofted to the upper portion of the cloud, whereas warm-CI clouds contain less cloud water at CI. Increased cloud water in the upper levels contributes to an increase in graupel formation near cloud top, which corresponds to the times of maximum growth and helps confirm that ice formation is a necessary component in CI and cloud growth leading to longer lasting storms. This also indicates that sustained condensation in the lower levels of the cloud is necessary to provide sustained sources of cloud water to be lofted into the upper portion of the convective clouds.

Using the 8.4 μm–10.35 μm BT differences, observed changes in *GOES-16* cloud top phase in CI events yield a positive BT difference trend that plateaus shortly after CI. The observed *GOES-16* BT does not reach full cloud top glaciation (BT differences remain < 0), but the positive trend provides evidence of the onset of ice and larger hydrometers at the cloud top. The CI cases from the Thompson microphysics scheme yield a similar result, whereas the Morrison and WDM6 schemes are too efficient at creating cloud ice particles (specifically graupel) and a glaciated cloud top (8.4 μm–10.35 μm BT difference switches to positive). Inspection of in-cloud mixing ratio profiles reveals that the Thompson scheme more readily converts cloud water to precipitation, whereas the Morrison scheme is able to loft more cloud water to higher levels, leading to increased graupel formation. When comparing cold-CI and warm-CI clouds, the cold bias from the Morrison scheme remains providing further evidence that it is producing too much graupel near the cloud top.

693 The application of observation-based CI techniques present a novel methodology to evaluate
694 high-resolution models with satellite data and examine the processes leading to CI development.
695 The results from this study illustrate that the model simulations are able represent cloud
696 evolution, but warm-CI clouds are too frequent. Previous radar-based studies that demonstrate
697 cloud tops with lower ice contents, such as those observed in the *GOES-16* ABI BT signatures
698 (Fig. 8), contain weaker updrafts (e.g. Matthee et al. 2014; Senf and Deneke 2017), which
699 suggests radar reflectivity due to warm rain. The lower level condensational growth and warm
700 rain processes are important for CI as early rain water partitioning in bulk microphysics can
701 impact downstream graupel production. Further, small rain hydrometeors have been found in
702 WDM6 using dual-polarized radar comparisons (e.g. Johnson et al. 2016; Lei et al. 2020), which
703 affects timing of CI detection. Bao et al. (2019) illustrate that differences in auto-conversion
704 parameterizations early in warm rain development can lead to downstream differences in graupel
705 production. The delay in rain formation in the WDM6 simulation and the increased graupel
706 formation when using the Morrison scheme suggests that insight into differences within auto-
707 conversion parameterizations could help sort differences in cloud evolution. Further analysis
708 comparing simulated cloud growth with clouds best matching GOES-16 observations could help
709 refine which auto-conversion rates are accurate in the cloud microphysics schemes. The
710 Thompson scheme most accurately describes the ice mixing ratios reaching cloud top at the time
711 of CI, but all of the parameterization schemes generally produce cloud tops that are too warm
712 early in development, thereby leading to higher growth rates before CI.
713 This is a single case study so additional case studies using satellite BTs and objected-based
714 methods to evaluate the characteristics of CI may be necessary to reinforce these findings.

Before CI was detected, IR BTs at cloud top were similar between warm-CI and cold-CI clouds in the WRF model simulations. This suggests that information content from cloud-top properties alone, such as ones utilized in geostationary-based CI forecasting, may be insufficient when forecasting CI during the early stages of cloud development when the convection is weakly forced. Additional simulations shedding light on other factors controlling the growth of simulated convection will be useful to aid in understanding the conditions optimal for CI growth in weakly forced cases. Future studies could concentrate on how the use of land surface models and planetary boundary layer schemes impact convective growth, updraft characteristics, and latent heating leading to CI. Finally, utilizing observations from ground-based active sensors that provide high resolution vertical profiles of hydrometeors and updrafts will be key in constraining model-based evaluations of convection. Such modeling studies are planned as well as observational analysis evaluating convective evolution using data from the Atmospheric Radiation Measurement (ARM) program matched to observed *GOES-16* CI cases.

Acknowledgments.

The authors would like to acknowledge the support by NSF Grant AGS-1746119 to complete this work. Further, we would like to thank Monica Harkey and Sarah Griffin from the University of Wisconsin for their support in WRF and CRTM development and Greg Thompson and Hugh Morrison at UCAR for useful conversations on microphysical evaluations. Finally, we thank the anonymous reviewers and editor for comments and suggestions that significantly improved the quality of this paper.

Data Availability Statement:

GOES-16 data used in this analysis can be downloaded from the National Oceanic and Atmospheric Administration Amazon Web Services (NOAA AWS; https://registry.opendata.aws/noaa-goes) data inventory. Ground-based NEXRAD radar data canbe downloaded from the National Climatic Data Center (https://www.ncdc.noaa.gov/data-access/radar-data). The authors have archived the WRF output data used in this study, as well as source codes for computing cloud positions, on a Space Science and Engineering server located at the University of Wisconsin. These files can be made available to anyone upon request.

6. References

Apke, J. M., J. R. Mecikalski, K. Bedka, E. W. McCaul, C. R. Homeyer, and C. P. Jewett, 2018: Relationships between Deep Convection Updraft Characteristics and Satellite-Based Super Rapid Scan Mesoscale Atmospheric Motion Vector–Derived Flow. Mon. Wea. Rev., 146, 3461–3480

Asefi-Najafabady, S., K. Knupp, J. R. Mecikalski, and R. M. Welch, 2012: Radar observations of mesoscale circulations induced by a small lake under varying synoptic-scale flows. J. Geophys. Res., 117, D01106.

Bao, J., S. A. Michelson, and E. D. Grell, 2019: Microphysical Process Comparison of Three Microphysics Parameterization Schemes in the WRF Model for an Idealized Squall-Line Case Study. Mon. Wea. Rev., 147, 3093–3120

Baum, B. A., P. F.Soulen, K. I.Strabala, M. D.King, S. A.Ackerman, W. P.Menzel, and P.Yang, 2000: Remote sensing of cloud properties using MODIS airborne simulator imagery during SUCCESS. 2. Cloud thermodynamic phase.J. Geophys. Res., 105, (D5). 11781–11792

Borbas, E. E., R. O.Knuteson, S. W.Seemann, E.Weisz, L.Moy, and H.-L.Huang, 2007: A high spectral resolution global land surface infrared emissivity database. Joint 2007 EUMETSAT Meteorological Satellite Conf. and the 15th Satellite Meteorology and Oceanography Conf. of the American Meteorological Society, Amsterdam, Netherlands,

Browning, K. A., and D. Atlas, 1965: Initiation of precipitation in vigorous convective clouds. J. Atmos. Sci., 22, 678–683.

Burghardt, B. J., C. Evans, and P. J. Roebber, 2014: Assessing the Predictability of Convection Initiation in the High Plains Using an Object-Based Approach. Wea. Forecasting, 29, 403–418

Bytheway, J. L., and C. D.Kummerow, 2018: Consistency between convection allowing model output and passive microwave satellite observations. J. Geophys. Res. Atmos., 123, 1065–1078

Bytheway, J. L., and C. D.Kummerow, 2015: Toward an object-based assessment of high-resolution forecasts of long-lived convective precipitation in the central U.S. J. Adv. Model. Earth Syst., 7, 1248–1264

Bytheway, J. L., C. D. Kummerow, and C. Alexander, 2017: A Features-Based Assessment of the Evolution of Warm Season Precipitation Forecasts from the HRRR Model over Three Years of Development. Wea. Forecasting, 32, 1841–1856

Cancelada, M.; Salio, P.; Vila, D.; Nesbitt, S.W.; Vidal, L., 2020: Backward Adaptive Brightness Temperature Threshold Technique (BAB3T): A Methodology to Determine Extreme Convective Initiation Regions Using Satellite Infrared Imagery. Remote Sens., 12, 337.

Cintineo, R., J. A.Otkin, M.Xue, and F.Kong, 2014: Evaluating the performance of planetary boundary layer and cloud microphysical parameterization schemes in convection permitting ensemble forecasts using synthetic GOES-13 satellite observations. Mon. Wea. Rev., 142, 163–182

798 Cintineo, J. L., M. J.Pavolonis, J. M.Sieglaff, and D. T.Lindsey, 2014: An empirical model for assessing
799 the severe weather potential of developing convection. Wea. Forecasting, 29, 639–653
800
801 Clark, A. J., R. G. Bullock, T. L. Jensen, M. Xue, and F. Kong, 2014: Application of Object-Based Time-
802 Domain Diagnostics for Tracking Precipitation Systems in Convection-Allowing Models. Wea.
803 Forecasting, 29, 517–542
804
805 Ding, S., P.Yang, F.Weng, Q.Liu, Y.Han, P.van Delst, J.Li, and B.Baum, 2011: Validation of the
806 Community Radiative Transfer Model. J. Quant. Spectrosc. Radiat. Transfer, 112, 1050–1064
807
808 Fiolleau, T., and R.Roca, 2013: An algorithm for the detection and tracking of tropical mesoscale
809 convective systems using infrared images from geostationary satellite. IEEE Trans. Geosci. Remote
810 Sens.,51, 4302–4315
811
812 Gambill, L. D., and J. R. Mecikalski, 2011: A satellite-based summer convective cloud frequency analysis
813 over the southeastern United States. J. Appl. Meteor. Climatol., 50, 1756–1769,
814
815 Goggins, G. D., M. L. Grantham, S. W. Unger, K. B. Laws, K. L. Pence, and L. Dawson, 2010: Analysis
816 of summer convection over central Alabama. Preprints, 15th Symp. on Meteorological Observation and
817 Instrumentation. Atlanta, GA, Amer. Meteor. Soc, 9.2
818
819 Grasso, L. D., and T.Greenwald, 2004: Analysis of 10.7-μm brightness temperatures of a simulated
820 thunderstorm with two-moment microphysics. Mon. Wea. Rev., 132, 815–825
821
822 Gravelle, C. M., J. R. Mecikalski, W. E. Line, K. M. Bedka, R. A. Petersen, J. M. Sieglaff, G. T. Stano,
823 and S. J. Goodman, 2016: Demonstration of a GOES-R Satellite Convective Toolkit to "Bridge the Gap"
824 between Severe Weather Watches and Warnings: An Example from the 20 May 2013 Moore, Oklahoma,
825 Tornado Outbreak. Bull. Amer. Meteor. Soc., 97, 69–84
826
827 Griffin, S. M., J. A. Otkin, C. M. Rozoff, J. M. Sieglaff, L. M. Cronce, and C. R. Alexander, 2017:
828 Methods for comparing simulated and observed satellite infrared brightness temperatures and what do
829 they tell us? Wea. Forecasting, 32, 5-25
830
831 Griffin, S. M., J. A. Otkin, G. Thompson, M. Frediani, J. Berner, and F. Kong, 2020: Assessing the
832 Impact of Stochastic Perturbations in Cloud Microphysics using GOES-16 Infrared Brightness
833 Temperatures. Mon. Wea. Rev., 148, 3111–3137
834
835 Han, D, J. Lee, J. Im, S. Sim, S. Lee, H. Han, 2019: A novel framework of detecting convective initiation
836 combining automated sampling, machine learning, and repeated model tuning from geostationary satellite
837 data Remote Sens., 11 p. 1454
838
839 Harris, R. J., J. R.Mecikalski, W. M.MacKenzie, P. A.Durkee, and K. E.Nielsen, 2010: The definition of
840 GOES infrared lightning initiation interest fields. J. Appl. Meteor. Climatol., 49, 2527–2543
841
842 Helmus, J.J. & Collis, S.M., 2016:The Python ARM Radar Toolkit (Py-ART), a Library for Working with
843 Weather Radar Data in the Python Programming Language. Journal of Open Research Software. 4(1),
844 p.e25
845
846 Hondl, K. D., and M. D. Eilts, 1994: Doppler radar signatures of developing thunderstorms and their
847 potential to initiate the onset of cloud–to–ground lightning. Mon. Wea. Rev., 122, 1818–1836.
848

Kain, J. S., and Coauthors, 2013: A Feasibility Study for Probabilistic Convection Initiation Forecasts Based on Explicit Numerical Guidance. Bull. Amer. Meteor. Soc., 94, 1213–1225,

Knight, C. A., and L. J. Miller, 1993: First radar echoes from cumulus clouds. Bull. Amer. Meteor. Soc., 74, 179–188.

Hong, Song–You, Yign Noh, Jimy Dudhia, 2006: A new vertical diffusion package with an explicit treatment of entrainment processes. Mon. Wea. Rev., 134, 2318–2341

Iacono, M. J., J. S. Delamere, E. J. Mlawer, M. W. Shephard, S. A. Clough, and W. D. Collins, 2008: Radiative forcing by long–lived greenhouse gases: Calculations with the AER radiative transfer models. J. Geophys. Res., 113

Johnson, M., Y. Jung, D. T. Dawson, and M. Xue, 2016: Comparison of Simulated Polarimetric Signatures in Idealized Supercell Storms Using Two-Moment Bulk Microphysics Schemes in WRF. Mon. Wea. Rev., 144, 971–996

Jones, T. A., and Coauthors, 2020: Assimilation of GOES-16 Radiances and Retrievals into the Warn-on-Forecast System. Mon. Wea. Rev., 148, 1829–1859

Kain, J. S., and Coauthors, 2008: Some practical considerations regarding horizontal resolution in the first generation of operational convection-allowing NWP. Wea. Forecasting, 23, 931–952

Kim, M., J. Jin, A. El Akkraoui, W. McCarty, R. Todling, W. Gu, and R. Gelaro, 2020: The Framework for Assimilating All-Sky GPM Microwave Imager Brightness Temperature Data in the NASA GEOS Data Assimilation System. Mon. Wea. Rev., 148, 2433–2455

Kirshbaum, D. J., F. Fabry, and Q. Cazenave, 2016: The Mississippi Valley convection minimum on summer afternoons: Observations and numerical simulations. Mon. Wea. Rev., 144, 263–272,

Langhans, W., J.Schmidli, O.Fuhrer, S.Bieri, and C.Schär, 2013: Long-term simulations of thermally-driven flows and orographic convection at convection-parameterizing and cloud-resolving resolutions. J. Appl. Meteor. Climatol.,52, 1490–1510.

Lee, S., Han, H., Im, J., Jang, E., & Lee, M.-I. 2017: Detection of deterministic and probabilistic convection initiation using Himawari-8 advanced Himawari imager data. Atmospheric Measurement Techniques

Lei, H., Guo, J., and Chen, D., 2020, Systematic bias in the prediction of warm-rain hydrometeors in the WDM6 microphysics scheme and modifications. Journal of Geophysical Research, in pres

Lim, K.-S. S., and S.-Y.Hong, 2010: Development of an effective double-moment cloud microphysics scheme with prognostic cloud condensation nuclei (CCN) for weather and climate models. Mon. Wea. Rev., 138, 1587–1612

Liu, H., and M.Xue, 2008: Prediction of convective initiation and storm evolution on 12 June 2002 during IHOP_2002. Part I: Control simulation and sensitivity experiments. Mon. Wea. Rev., 136, 2261–2282

Lopez, P., K.Finkele, P.Clark, and P.Mascart, 2003: Validation and intercomparison of three FASTEX cloud systems: Comparison with coarse-resolution simulations.Quart. J. Roy. Meteor. Soc., 129, 1841–1871

Mace, G. G., and F. J.Wrenn, 2013: Evaluation of the hydrometeor layers in the east and west Pacific within ISCCP cloud-top pressure–optical depth bins using merged CloudSat and CALIPSO data. J. Climate, 26, 9429–9444

Madaus, L. E., and G. J.Hakim, 2016: Observable surface anomalies preceding simulated isolated convective initiation. Mon. Wea. Rev., 144, 2265–2284

Madaus, L. E., and G. J. Hakim, 2017: Constraining Ensemble Forecasts of Discrete Convective Initiation with Surface Observations. Mon. Wea. Rev., 145, 2597–2610

Marshall, J. S., and S. Radhakant, 1978: Radar precipitation maps as lightning indicators. J. Appl. Meteorol., 17, 206–212.

Mecikalski, J. R., and K. M.Bedka, 2006: Forecasting convective initiation by monitoring the evolution of moving cumulus in daytime GOES imagery.Mon. Wea. Rev., 134, 49–78

Mecikalski, J. R., K.Bedka, S.Paech, and L.Litten, 2008: A statistical evaluation of GOES cloud-top properties for nowcasting convective initiation.Mon. Wea. Rev., 136, 4899–4914

Mecikalski, J. R., W. M. Mackenzie, M. Koenig, and S. Muller, 2010a: Use of Meteosat Second Generation infrared data in 0-1 hour convective initiation nowcasting. Part 1. Infrared fields. J. Appl. Meteor. Climate., 49, 521-534.

Mecikalski, J. R., W. M.Mackenzie, M.Koenig, and S.Muller, 2010b: Cloud-top properties of growing cumulus prior to convective initiation as measured by Meteosat Second Generation. Part I: Infrared fields. J. Appl. Meteor. Climatol., 49, 521–534

Mecikalski, J. R., P. Minnis, and R. Palikonda, 2013: Use of satellite derived cloud properties to quantify growing cumulus beneath cirrus clouds. Atmos. Res., 120-121, 192-201

Mecikalski, J. R., J. K. Williams, C. P. Jewett, D. Ahijevych, A. LeRoy, and J. R. Walker, 2015: Probabilistic 0–1-h Convective Initiation Nowcasts that Combine Geostationary Satellite Observations and Numerical Weather Prediction Model Data. J. Appl. Meteor. Climatol., 54, 1039–1059

Mecikalski, J. R., D. Rosenfeld, and A. Manzato, 2016a: A conceptual model for 1–2 hour nowcasts of storm intensity using geostationary satellite observations. J. Geophys. Res. Atmos., 121, 6374–6392.

Mecikalski, J. R., C. P. Jewett, J. M. Apke, and L. D. Carey, 2016b: Analysis of cumulus cloud updrafts as observed with 1–min resolution super rapid scan GOES imagery. Mon. Wea. Rev., 144, 811–830.

Miller, P. W., and T. L. Mote, 2017: A climatology of weakly forced and pulse thunderstorms in the southeast United States. J. Appl. Meteor. Climatol., 56, 3017–3033, https://doi.org/ 10.1175/JAMC-D-17-0005.1.

Mittermaier, M. and R. Bullock, 2013: Using MODE to explore the spatial and temporal characteristics of cloud cover forecasts from high-resolution NWP models. Meteor. Appl., 20, 187–196

Morrison, H., J. A.Curry, and V. I.Khvorostyanov, 2005: A new double-moment microphysics parameterization for application in cloud and climate models. Part I: Description. J. Atmos. Sci., 62, 1665–1677

Mueller, C. K., J. W. Wilson, and N. A. Crook, 1993: The utility of sounding and mesonet data to nowcast thunderstorm initiation. Wea. Forecasting, 8, 132–146.

Mueller, C., T. Saxen, R. Roberts, J. Wilson, T. Betancourt, S. Dettling, N. Oien, and J. Yee, 2003: NCAR Auto-Nowcast system. Wea. Forecasting, 18, 545–561.

Niu, Guo–Yue, Zong–Liang Yang, Kenneth E. Mitchell, Fei Chen, Michael B. Ek, Michael Barlage, Anil Kumar, Kevin Manning, Dev Niyogi, Enrique Rosero, Mukul Tewari, Youlong Xia, 2011: The community Noah land surface model with multiparameterization options (Noah–MP): 1. Model description and evaluation with local–scale measurements. J. Geophys. Res., 116, D12109

Otkin, J. A., and T. J.Greenwald, 2008: Comparison of WRF model-simulated and MODIS-derived cloud data. Mon. Wea. Rev., 136, 1957–1970

Otkin, J. A., T. J. Greenwald, J. Sieglaff, and H.-L. Huang, 2009: Validation of a large-scale simulated brightness temperature dataset using SEVIRI satellite observations. J. Appl. Meteor. Climatol., 48, 1613-1626

Patou, M., J. Vidot, J. Riédi, G. Penide, and T. J. Garrett, 2018: Prediction of the Onset of Heavy Rain Using SEVIRI Cloud Observations. J. Appl. Meteor. Climatol., 57, 2343–2361

Rickenbach, T. M., R.Nieto-Ferreira, C.Zarzar, and B.Nelson, 2015: A seasonal and diurnal climatology of precipitation organization in the southeastern United States. Quart. J. Roy. Meteor. Soc., 141, 1938–1956

Rickenbach, T.M., R.N. Ferreira, and H. Wells, 2020: Springtime Onset of Isolated Convection Precipitation across the Southeastern United States: Framework and Regional Evolution. Mon. Wea. Rev., 148, 891–906,

Roberts, R. D., and S.Rutledge, 2003: Nowcasting storm initiation and growth using GOES-8 and WSR-88D data.Wea. Forecasting, 18, 562–584

Schmit, T. J., P.Griffith, M. M.Gunshor, J. M.Daniels, S. J.Goodman, and W. J.Lebair, 2017: A closer look at the ABI on the GOES-R series. Bull. Amer. Meteor. Soc., 98, 681–698, https://doi.org/10.1175/BAMS-D-15-00230.1

Schreiber, W. E., 1986: Case study of thunderstorms initiated by radar-observed convergence lines. Mon. Wea. Rev., 114, 2256–2266.

Schwartz, C. S., and Coauthors, 2009: Next-day convection-allowing WRF model guidance: A second look at 2-km versus 4-km grid spacing. Mon. Wea. Rev., 137, 3351–3372

Senf, F., and H. Deneke, 2017: Satellite-Based Characterization of Convective Growth and Glaciation and Its Relationship to Precipitation Formation over Central Europe. J. Appl. Meteor. Climatol., 56, 1827–1845

Sieglaff, J. M., L. M.Cronce, W. F.Feltz, K. M.Bedka, M. J.Pavolonis, and A. K.Heidinger, 2011: Nowcasting convective storm initiation using satellite-based box-averaged cloud-top cooling and cloud-type trends. J. Appl. Meteor. Climatol., 50, 110–126

Sobash, R. A., and D. J.Stensrud, 2015: Assimilating surface mesonet observations with the EnKF to improve ensemble forecasts of convection initiation on 29 May 2012. Mon. Wea. Rev., 143, 3700–3725

Song, H.-J., and B. J.Sohn, 2018: An evaluation of WRF microphysics schemes for simulating the warm-type heavy rain over the Korean peninsula. Asia-Pac. J. Atmos. Sci., 54, 1–12

Tiedtke, M., 1989: A comprehensive mass flux scheme for cumulus parameterization in large–scale models. Mon. Wea. Rev., 117, 1779–1800.

Thompson, G., P. R.Field, R. M.Rasmussen, and W. D.Hall, 2008: Explicit forecasts of winter precipitation using an improved bulk microphysics scheme. Part II: Implementation of a new snow parameterization.Mon. Wea. Rev., 136, 5095–5115

Thompson, G., M.Tewari, K.Ikeda, S.Tessendorf, C.Weeks, J.Otkin, and F.Kong, 2016: Explicitly-coupled cloud physics and radiation parameterizations and subsequent evaluation in WRF high-resolution convective forecasts. Atmos. Res., 168, 92–104

Tselioudis, G., and C.Jakob, 2002: Evaluation of midlatitude cloud properties in a weather and a climate model: Dependence on dynamic regime and spatial resolution.J. Geophys. Res., 107, 4781

Vila, D. A., L. A. T. Machado, H. Laurent, and I. Velasco, 2008: Forecast and Tracking the Evolution of Cloud Clusters (ForTraCC) Using Satellite Infrared Imagery: Methodology and Validation. Wea. Forecasting, 23, 233–245

P. Virtanen, R. Gommers, T. E. Oliphant at al.2020: SciPy 1.0–fundamental algorithms for scientific computing in PYTHON,
Nature Methods 17, 261

Walker, J. R., W. M.MacKenzie, J. R.Mecikalski, and C. P.Jewett, 2012: An enhanced geostationary satellite–based convective initiation algorithm for 0–2-h nowcasting with object tracking. J. Appl. Meteor. Climatol., 51, 1931–1949

Wall, C. J., D. L. Hartmann, M. M. Thieman, W. L. Smith, and P. Minnis, 2018: The Life Cycle of Anvil Clouds and the Top-of-Atmosphere Radiation Balance over the Tropical West Pacific. J. Climate, 31, 10059–10080

Weckwerth, T. M., and R. M. Wakimoto, 1992: The initiation and organization of convective cells atop a cold–air outflow boundary. Mon. Wea. Rev., 120, 2169–2187.

Weckwerth, T. M., and D. B.Parsons, 2006: A review of convective initiation and motivation for IHOP_2002.Mon. Wea. Rev, 134, 5–22

Weisman, M. L., C.Davis, W.Wang, K. W.Manning, and J. B.Klemp, 2008: Experiences with 0-36-h explicit convective forecasts with the WRF-ARW model. Wea. Forecasting, 23, 407–437

Wilson, J. W., and W. E. Schriber, 1986: Initiation of convective storms by radar–observed boundary layer convergent lines. Mon. Wea. Rev., 114, 2516–2536.

Wilson, J. W., and C. K. Mueller, 1993: Nowcasts of thunderstorm initiation and evolution. Wea. Forecasting, 8, 113–131.

Wilson, J. W., G. B. Foote, N. A. Crook, J. C. Fankhauser, C. G. Wade, J. D. Tuttle, C. K. Mueller, and S. K. Kruger, 1992: The role of boundary–layer convergence zones and horizontal rolls in the initiation of thunderstorms. A case study. Mon. Wea. Rev., 120, 1785–1815.

Yussouf, N., D. C. Dowell, L. J. Wicker, K. H. Knopfmeier, and D. M. Wheatley, 2015: Storm-Scale Data Assimilation and Ensemble Forecasts for the 27 April 2011 Severe Weather Outbreak in Alabama. Mon. Wea. Rev., 143, 3044–3066

Zhang, Chunxi, Yuqing Wang, and Kevin Hamilton, 2011: Improved representation of boundary layer clouds over the southeast pacific in ARW–WRF using a modified Tiedtke cumulus parameterization scheme. Mon. Wea. Rev., 139, 3489–3513

Zhang, Y., D. J. Stensrud, and F. Zhang, 2019: Simultaneous Assimilation of Radar and All-Sky Satellite Infrared Radiance Observations for Convection-Allowing Ensemble Analysis and Prediction of Severe Thunderstorms. Mon. Wea. Rev., 147, 4389–4409

Zipser, E. J., 2003: Some views on "hot towers" after 50 years of tropical field programs and two years of TRMM data. Cloud Systems, Hurricanes, and the Tropical Rainfall Measuring Mission (TRMM), Meteor. Monogr., No. 51, Amer. Meteor. Soc., 49–58

Tables and Figures

	Total Cloud Objects BT <285K	# CI Tracked	Time First CI
GOES-16	546	52	1655 UTC
Thompson	1853	121	1645 UTC
Morrison	2160	136	1650 UTC
WDM6	1946	67	1700 UTC

Table 1. Number of total cloud objects colder than 285 K, number of CI objects tracked, and time of first tracked CI cloud in the *GOES-16* observations and the Thompson, Morrison, and WDM6 simulations.

Time [UTC]	1700	1800	1900	2000
GOES-16	257.6	241.2	228.6	217.5
Thompson	256.3	237.8	223.1	214.8
Morrison	254.5	240.3	229.6	216.5
WDM6	260.1	241.5	227.8	218.4

Table 2. The 10th percentile of the 10.3 μm BT distributions for the *GOES-16* observations and Thompson, Morrison, and WDM6 simulations at 1700 UTC, 1800 UTC, 1900 UTC, and 2000 UTC.

	Time-lag from CI [mins]	Thompson	Morrison	WDM6	WDM6-lagged
10.35 μm	–15	3.45	3.28	–16.23	–1.51
	–10	2.78	2.03	–16.31	–3.81
	–5	0.34	–1.1	–20.02	–3.73
	0	–3.48	–1.98	–19.93	–2.41
	+5	–2.65	–2.61	–20.67	–0.61
	+10	–1.33	–1.95	–23.52	–2.91
	+15	–0.35	–1.13	–24.02	–2.52
	Time-lag from CI [mins]	**Thompson**	**Morrison**	**WDM6**	**WDM6-lagged**
10.35 μm tendency	–10	–1.16	–1.65	–2.65	–2.12
	–5	–1.66	–2.39	0.55	–2.41
	0	–3.96	–0.95	1.11	–1.72
	+5	–0.88	–1.45	–0.14	–0.65
	+10	1.75	0.75	–1.63	–1.04
	+15	0.47	1.76	1.39	0.14

Table 3. Differences of the mean BT (Model–Obs) of the (top) 10.35 μm BT and (bottom) 8.4–10.35 μm BT tendency computed using the mean of the interquartile range. Differences are given for timesteps before and after CI is detected. All units are [K].

	Total Cloud Objects BT < 285K	Cloud objects with dBZ ≥ 35	Cloud objects reaching 250 K	Cloud objects that do not reach 250 K
GOES-16	546	52	31	21
Thompson	1853	121	46	75
Morrison	2160	136	52	84

Table 4. Number of total cloud objects with 10.35 μm brightness temperature < 285 K, number of CI cloud objects meeting the 35 dBZ criterion, number of CI cloud objects meeting the 35 dBZ and 250 K criterion, and the number of CI cloud objects meeting the 35 dBZ criterion but not the 250 K criterion. Results are shown for the *GOES-16* observations and the Thompson and Morrison simulations.

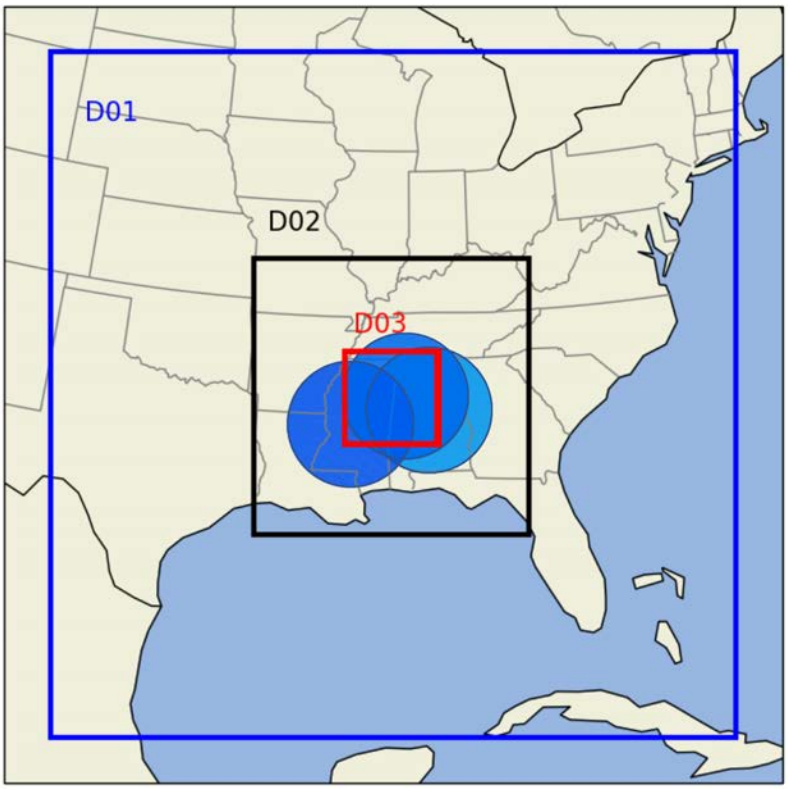

Figure 1. Illustration of the three WRF model domains. Convective initiation is assessed within the inner domain (D03) using *GOES-16* observations and data from three WSR-88D radar sites (blue circles).

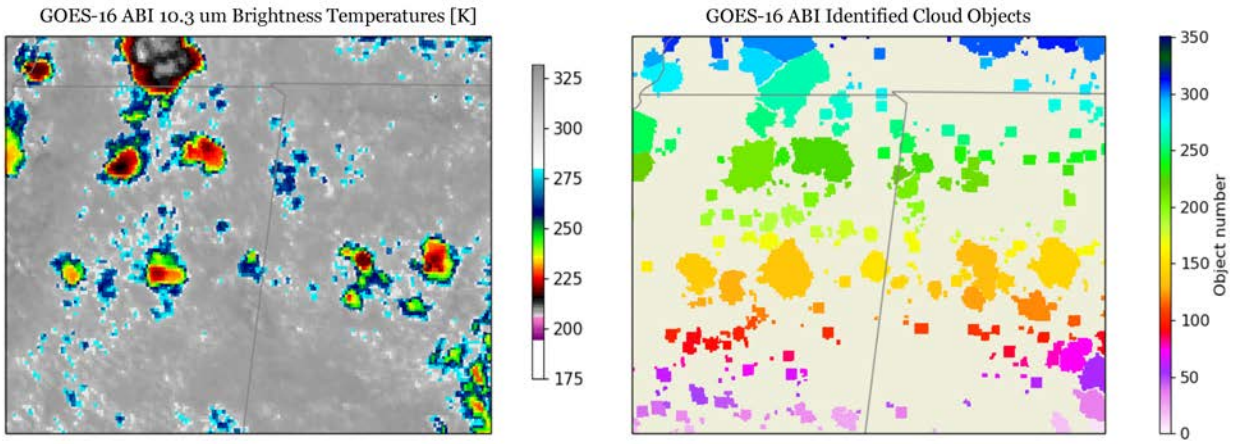

Figure 2. An example of (left) 1900 UTC *GOES-16 ABI* 10.35 μm brightness temperatures [K] within the inner domain region. (right) Derived cloud objects from this timestep.

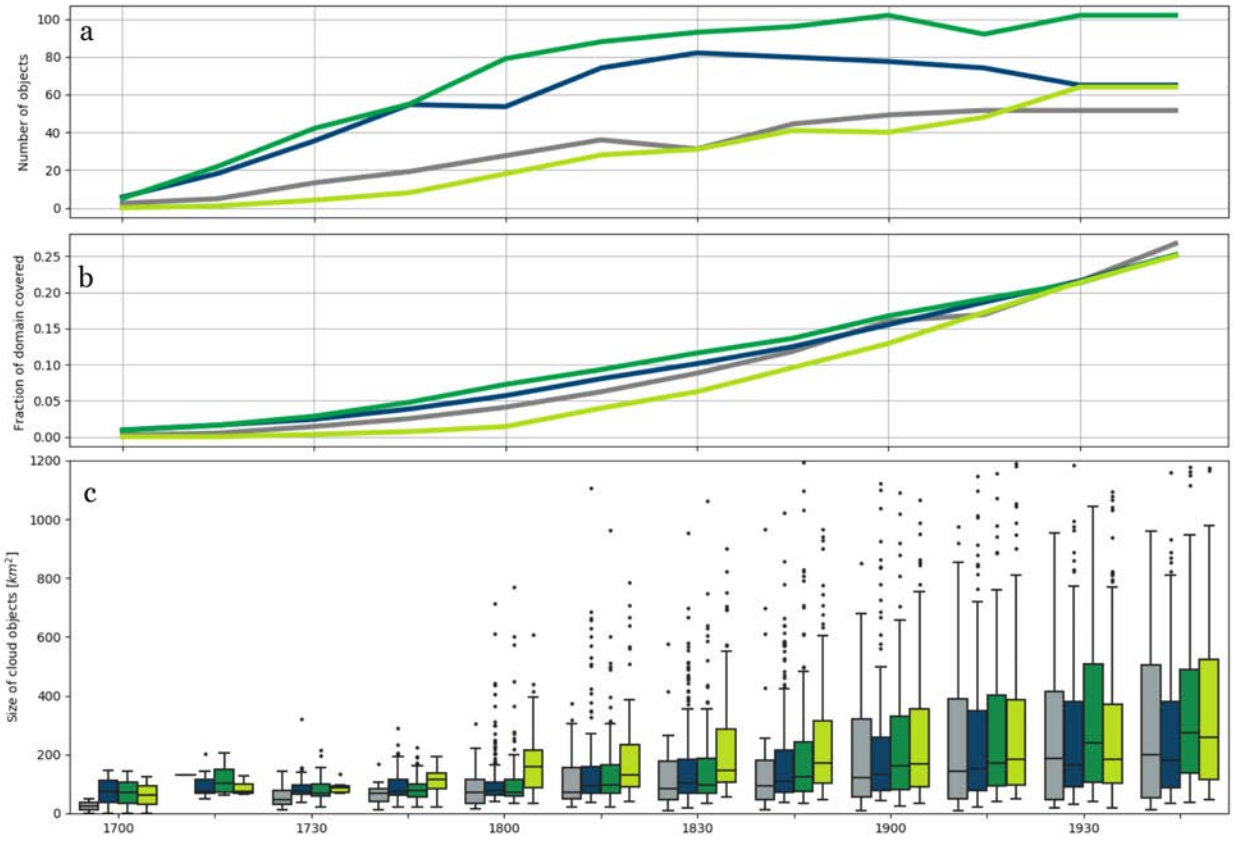

Figure 3. The (a) occurrence of active CI cloud objects containing a reflectivity higher than 35 dBZ at each timestep (b) fractional coverage of active CI cloud objects, and (c) sizes of CI cloud objects for *GOES-16* (grey) observations and Thompson (blue), Morrison (green), and WDM6 (light green) simulations. Occurrence is shown by the solid lines and the spread of cloud object sizes is shown using the box and whisker diagrams.

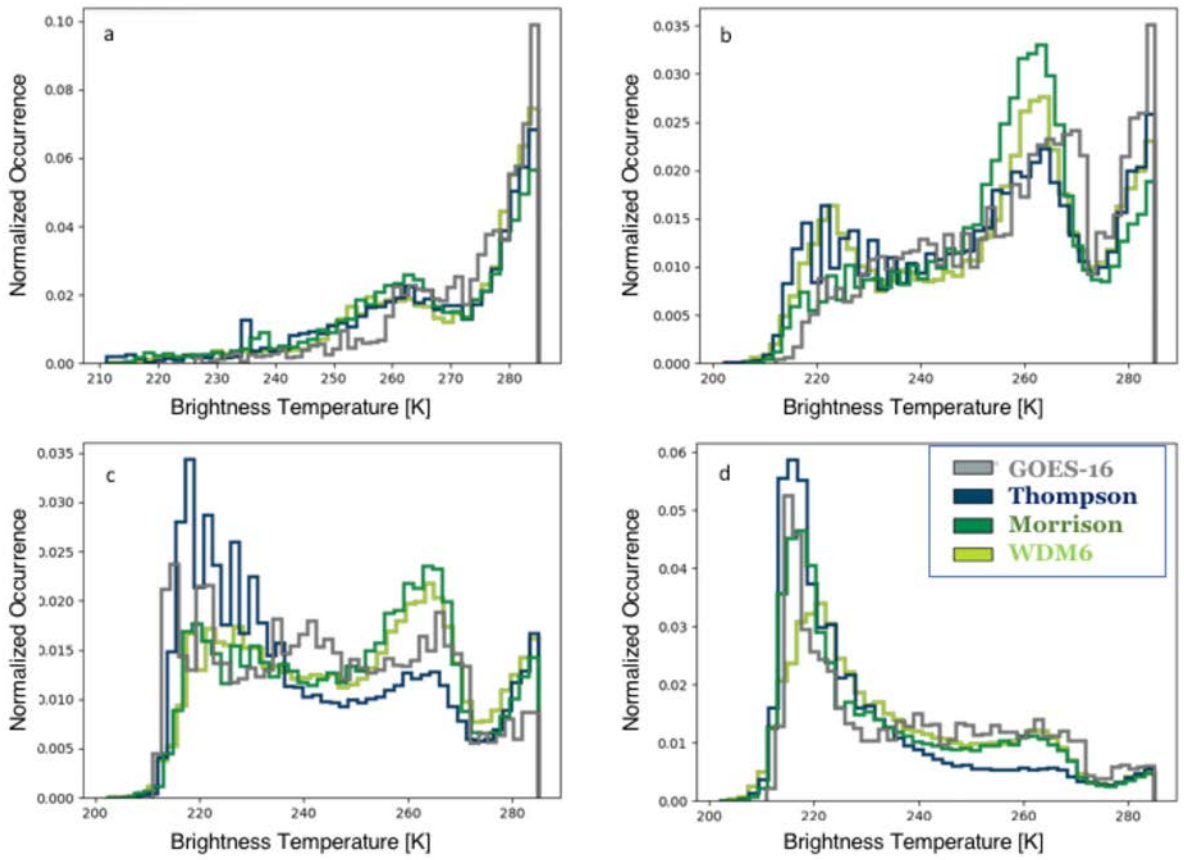

Figure 4. Normalized ABI 10.35 μm brightness temperature probability density functions at (a) 1700 UTC (b) 1800 UTC (c) 1900 UTC and (d) 2000 UTC. Brightness temperatures are binned every 2 K for *GOES-16* (grey) observations and Thompson (blue), Morrison (green), and WDM6 (light green) simulations

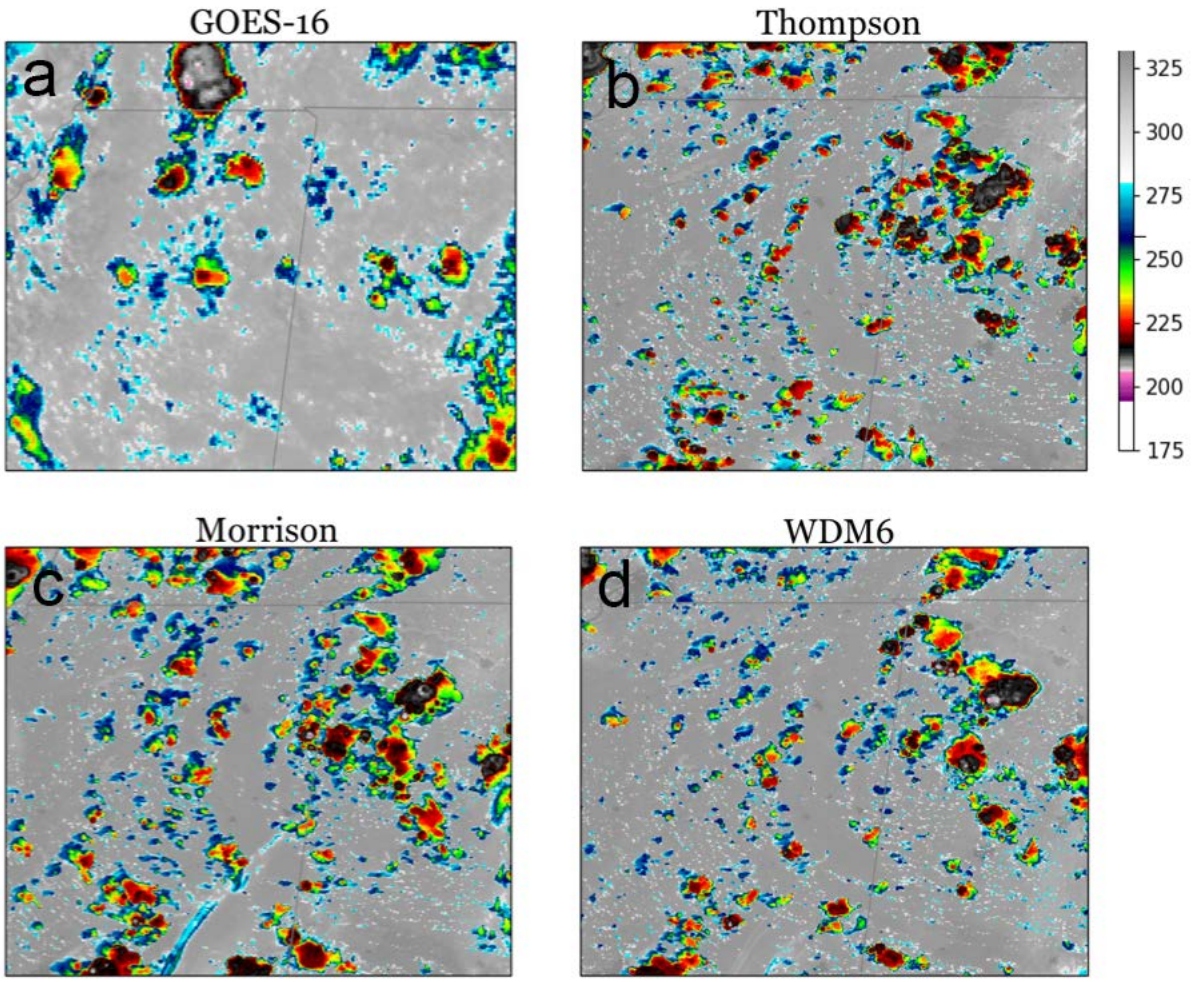

Figure 5. Observed and simulated ABI 10.35 μm brightness temperatures [K] at 1900 UTC for (a) *GOES-16*, (b) Thompson, (c) Morrison, and (d) WDM6.

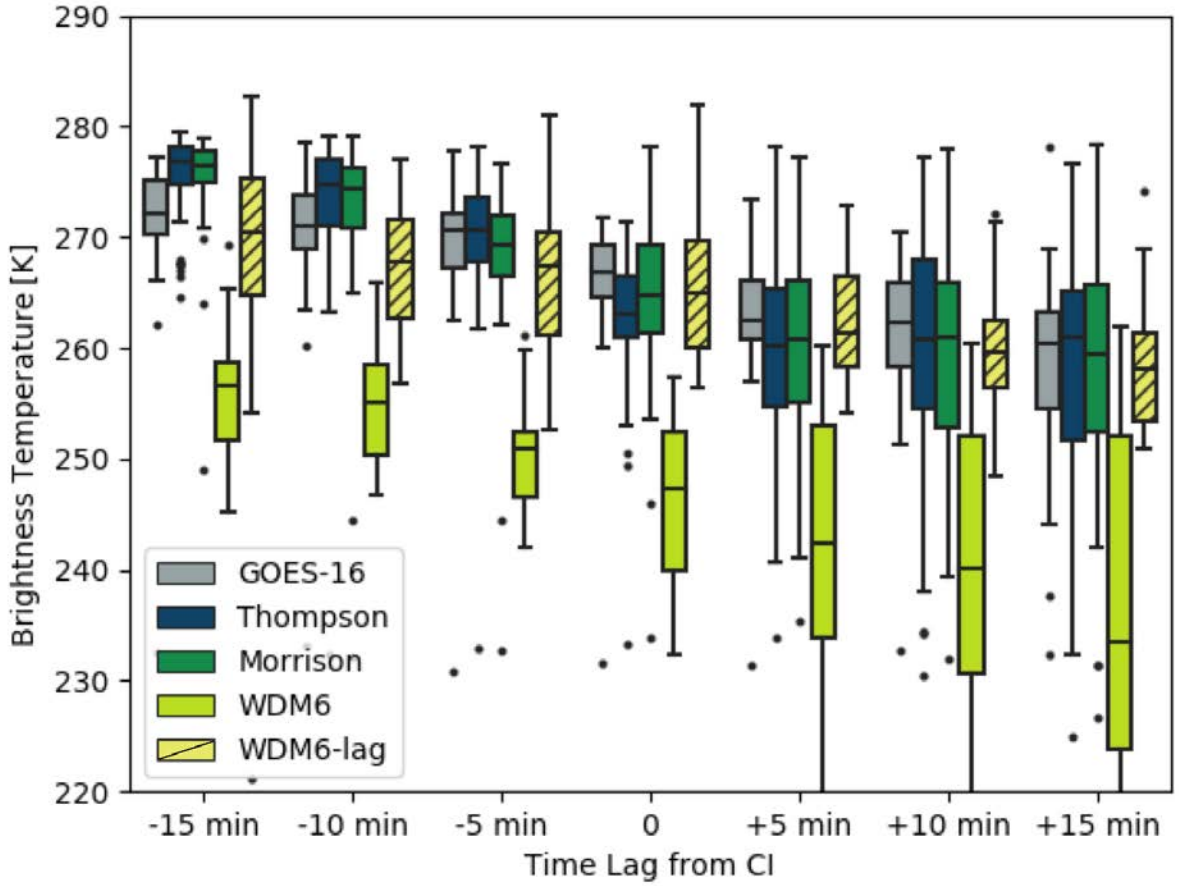

Figure 6. Box and Whisker plots of ABI 10.35 μm brightness temperatures [K] for *GOES-16* (grey), Thompson (blue), Morrison (green), WDM6 (light green), and WDM6 lagged 30 minutes (hatched). Bars are spaced at 5-minute intervals with time = 0 defined as the time CI was detected.

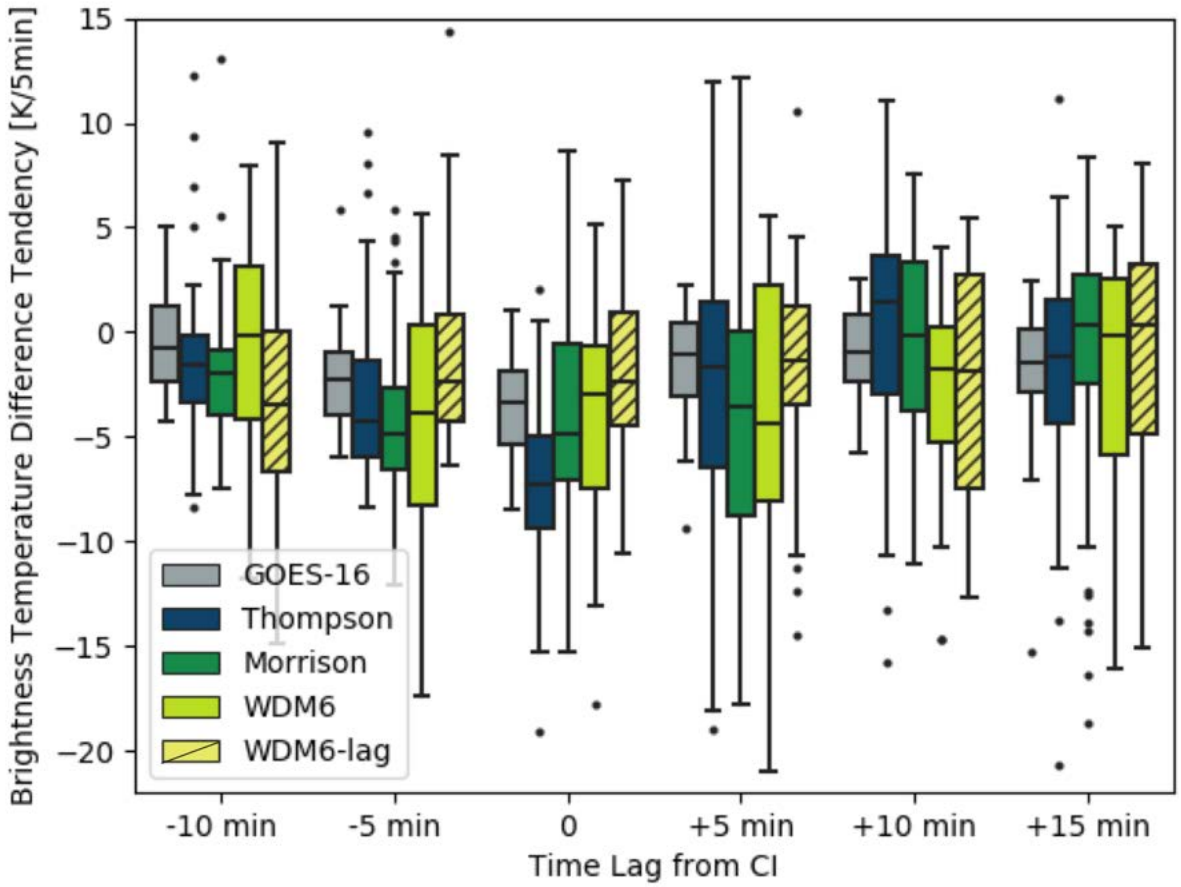

Figure 7. Box and Whisker plots for the ABI 10.35 μm brightness temperature growth tendency field for *GOES-16* (grey), Thompson (blue), Morrison (green), WDM6 (light green), and WDM6 lagged 30 minutes (hatched). Bars are spaced at 5-minute intervals with Time = 0 defined as the time CI was detected. Each tendency is the change in BT between the listed time-step and timestep before.

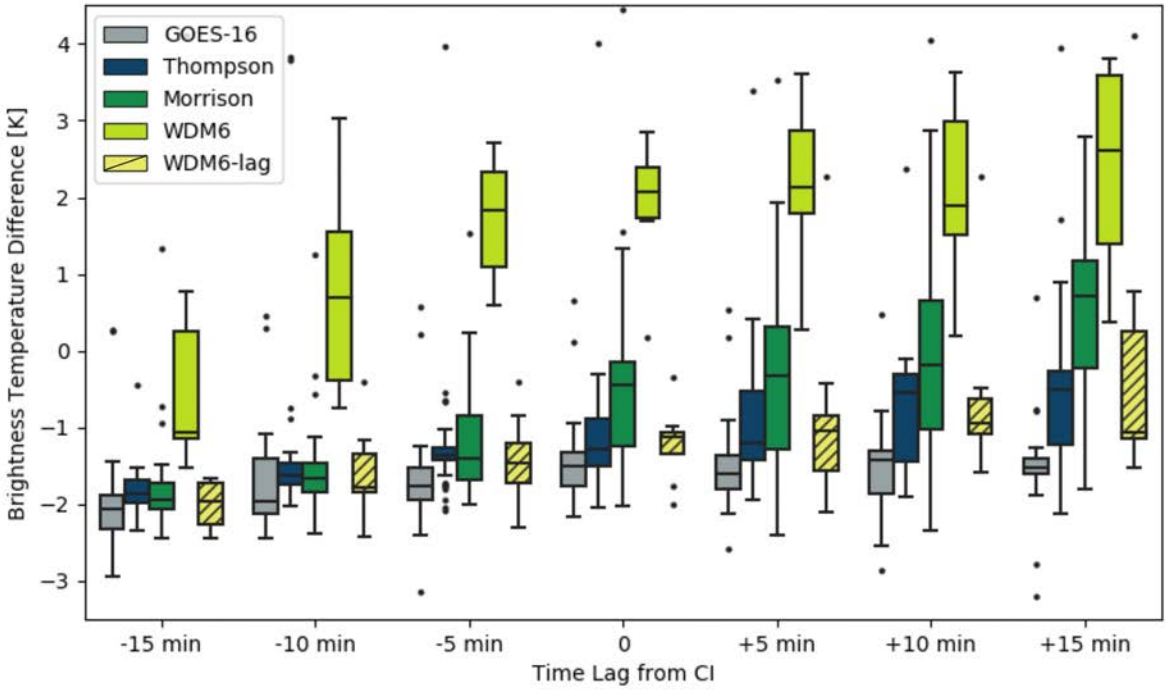

Figure 8. Same as Figure 6 except for showing ABI 8.4–10.35 μm brightness temperature differences [K].

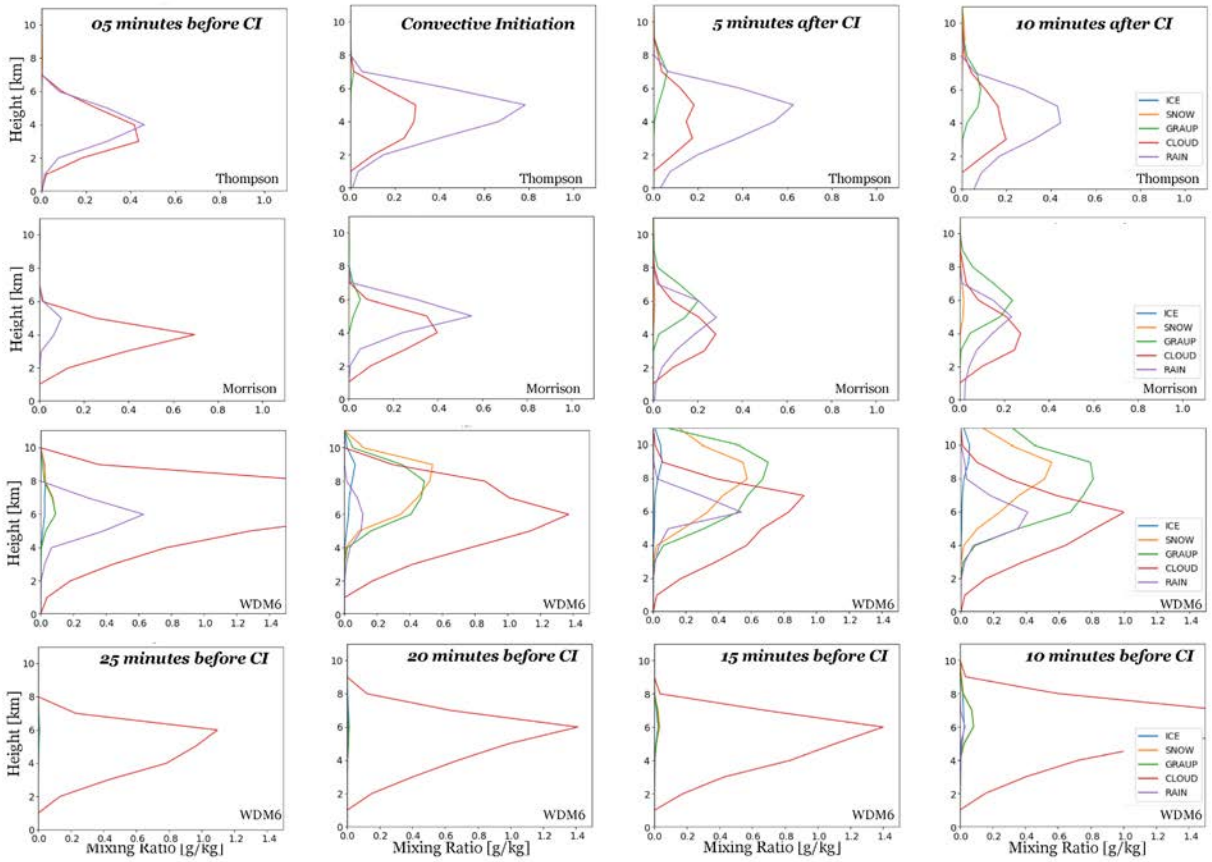

Figure 9. Evolution of mean profiles for ice, snow, graupel, cloud water, and rain water mixing ratios from 5 min before CI until 10 min after CI was identified. Profiles are shown for Thompson (first row), Morrison (second row), and WDM6 (bottom rows) bulk microphysics schemes. The bottom row contains WDM6 profiles lagged an additional 20 mins.

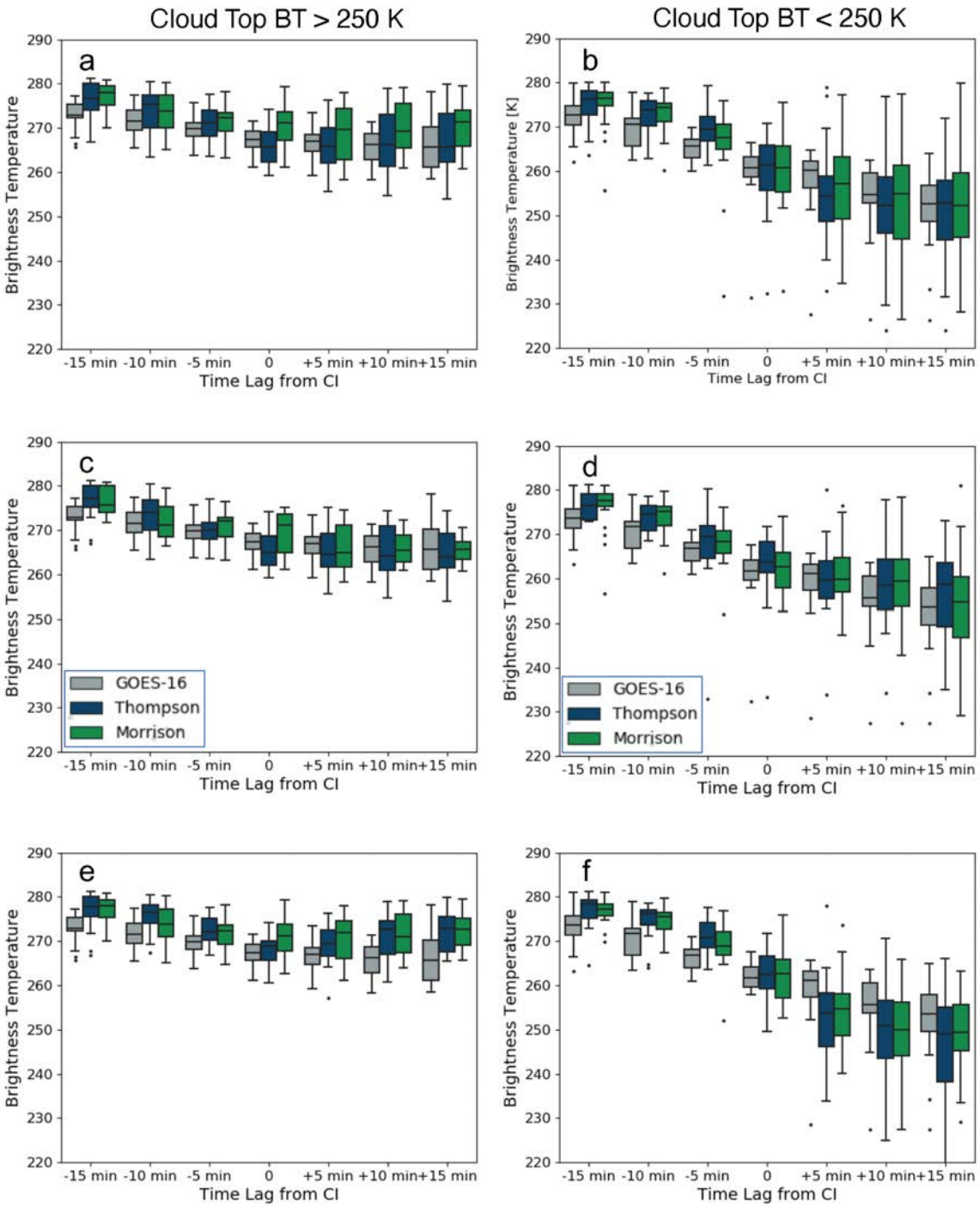

Figure 10. Same as Fig. 6, but for cases subset into warm-CI clouds and cold-CI clouds. (left) warm-CI clouds for (a) all cases, (c) top 50% best-matched cases, and (e) cases outside 50% best-matched. (left) cold-CI clouds for (b) all cases, (d) top 50% best-matched cases, and (f) cases outside 50% best-matched. Results are shown for the Thompson (blue) and Morrison (green) simulations.

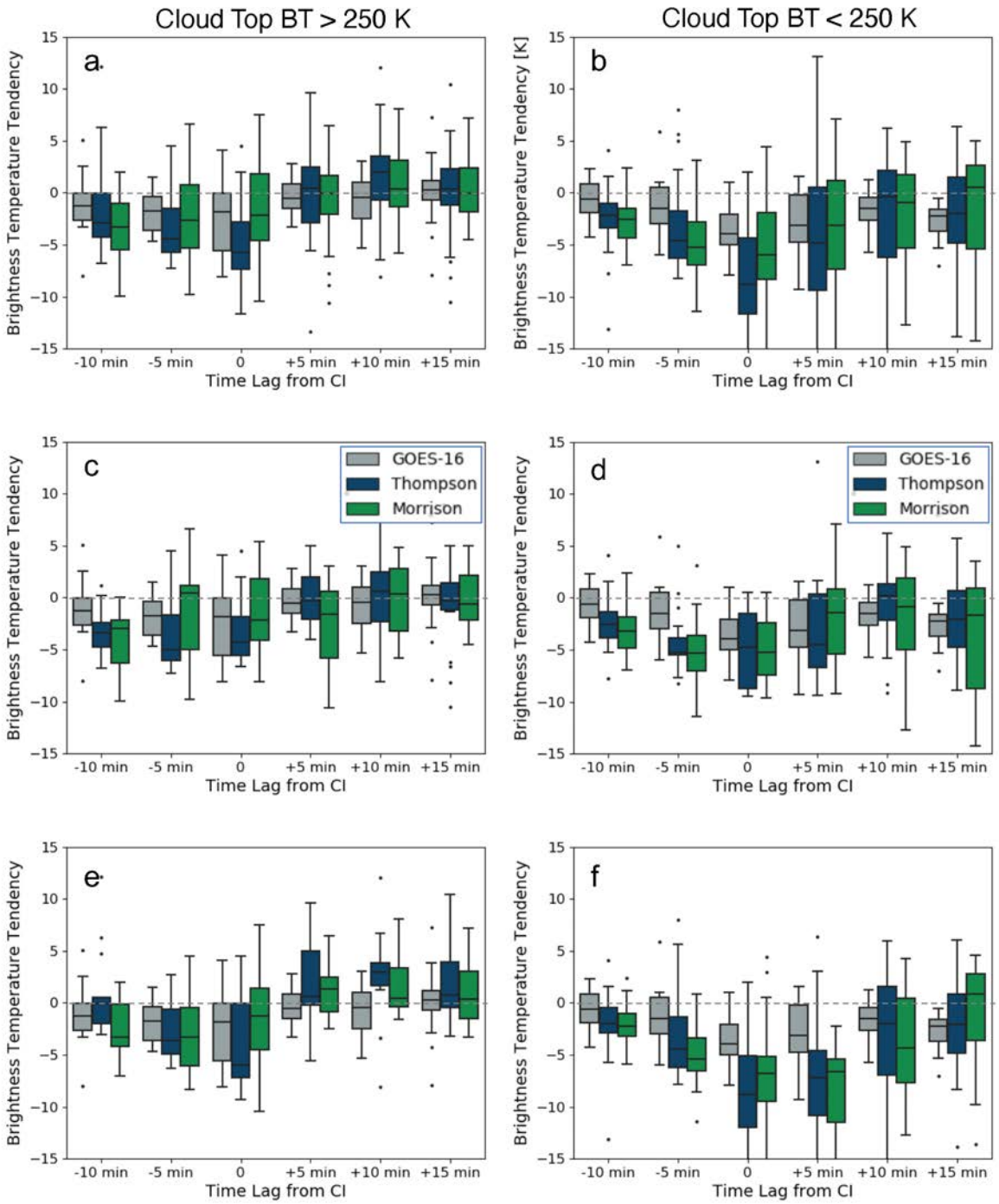

Figure 11. Same as Figure 7, but for cases subset into warm-CI clouds and cold-CI clouds. (left) warm-CI clouds for (a) all cases, (c) top 50% best-matched cases, and (e) cases outside 50% best-matched. (left) cold-CI clouds for (b) all cases, (d) top 50% best-matched cases, and (f) cases outside 50% best-matched. Results are shown for the Thompson (blue) and Morrison (green) simulations.

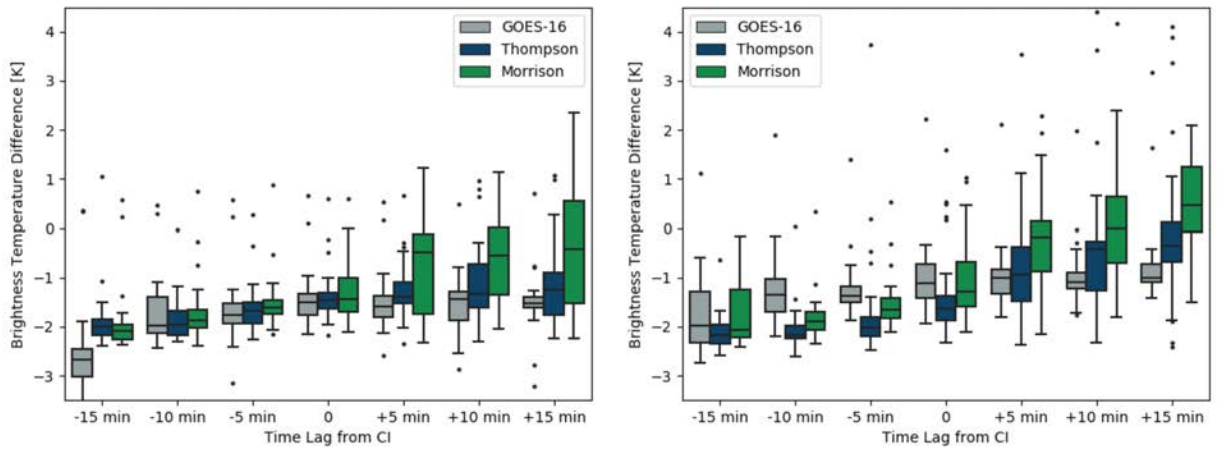

Figure 12. The ABI 8.4–10.3 μm BT difference to evaluate cloud top glaciation for cases subset into (left) warm-CI clouds and (right) cold-CI clouds. Results are shown for the Thompson (blue) and Morrison (green) simulations.

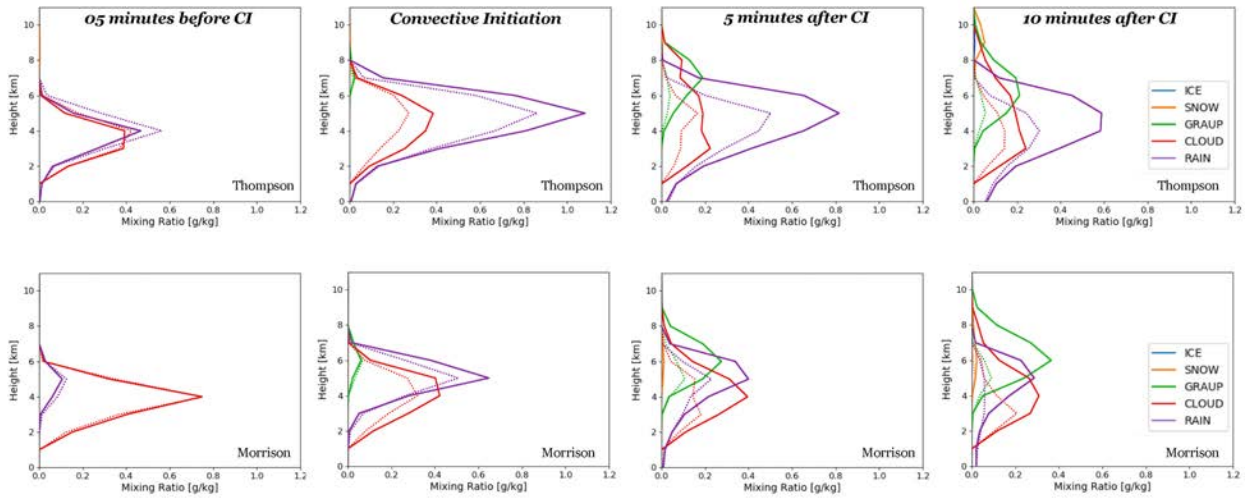

Figure 13. Evolution of mean profiles for ice, snow, graupel, cloud water, and rainwater mixing ratios from 5 min before CI until 10 min after CI was identified. Profiles are shown for Thompson (top row) and Morrison (bottom row) simulations for cold-CI clouds (solid lines) and warm-CI clouds (dotted lines).

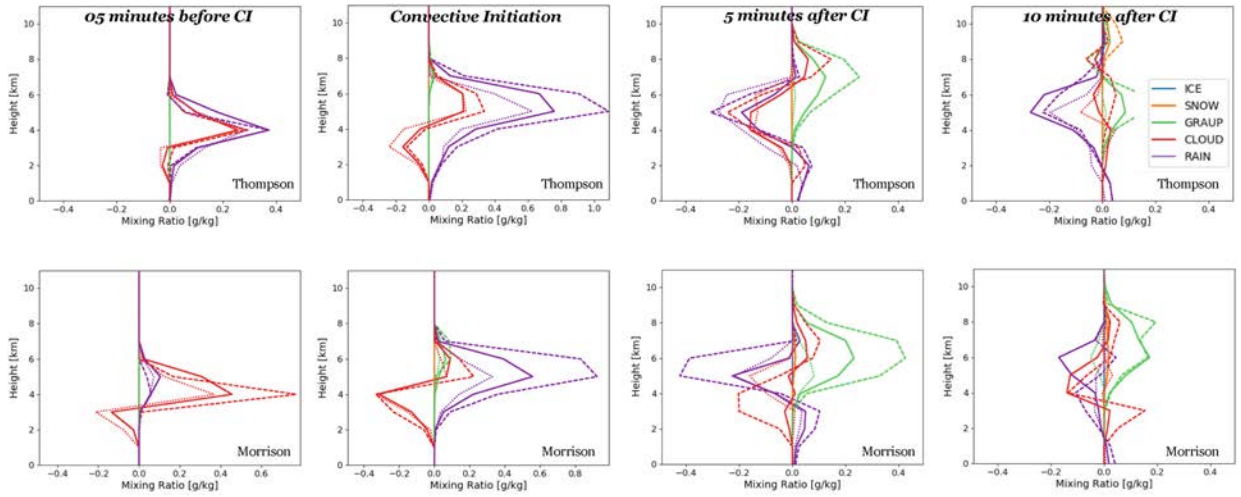

Figure 14. Evolution of mean in cloud tendency profiles of ice, snow, graupel, cloud water, and rainwater mixing ratios from 5 min before CI until 10 min after CI was observed. Profiles are shown for the Thompson (top row), and Morrison (bottom row) simulations. The growth categories are shown for warm-CI clouds (dotted lines), best-matched cases cold-CI clouds (solid lines), and growth cold-CI clouds (dashed line).